View metadata, citation and similar papers at core.ac.uk

brought to you by CORE

provided by Michigan Technological University

Michigan Technological University

Digital Commons @ Michigan Tech

Dissertations, Master's Theses and Master's Reports - Open

Dissertations, Master's Theses and Master's Reports

2006

Emission cross sections for neutral xenon impacted by Xe^{+} and Xe^{2+}

Jason D. Sommerville

Michigan Technological University

Follow this and additional works at: https://digitalcommons.mtu.edu/etds

 Part of the Mechanical Engineering Commons

Copyright 2006 Jason D. Sommerville

Recommended Citation

Sommerville, Jason D., "Emission cross sections for neutral xenon impacted by Xe^{+} and Xe^{2+}", Master's Thesis, Michigan Technological University, 2006.
https://digitalcommons.mtu.edu/etds/412

Follow this and additional works at: https://digitalcommons.mtu.edu/etds

 Part of the Mechanical Engineering Commons

Emission Cross Sections for Neutral Xenon Impacted by Xe^{+} and Xe^{2+}

by

Jason D. Sommerville

A Thesis

Submitted in partial fulfillment of the requirements for the degree of
Master of Science in Mechanical Engineering

MICHIGAN TECHNOLOGICAL UNIVERSITY
2006

Copyright © 2006 Jason D. Sommerville

MICHIGAN TECHNOLOGICAL UNIVERSITY

Department of Mechanical Engineering-Engineering Mechanics

This thesis entitled *Emission cross sections for Neutral Xenon Impacted by Xe^{+} and Xe^{2+}* by Jason D. Sommerville is hereby accepted in partial fulfillment of the requirements for the degree of Master of Science in Mechanical Engineering.

Signed:

Thesis Advisor: Dr. Lyon B. King Date

Department Chair: Dr. William W. Predebon Date

To my wife

Renata

for your support and flexibility while I live the life of a graduate student. You are my workmate, playmate, lifemate, and soulmate.

Abstract

Ion impact emission cross sections for eleven transitions from the $5p^5 6p$ configuration to the $5p^5 6s$ configuration of neutral xenon occurring in the spectral region between 700 nm and 1000 nm have been measured experimentally. Collisions between both singly- and doubly-ionized xenon and neutral xenon have been studied. These cross sections are of primary use in the development of a spectrographic diagnostic for Hall effect thruster plasma. A detailed discussion of the experimental methods and the subsequent data reduction is included. The results are presented and the importance of these data for spectrographic emission models of Hall effect thruster plasmas is discussed.

Acknowledgments

I conducted these experiments under the guidance of Dr. Rainer A. Dressler and Dr. Yu-Hui Chiu, both of the Air Force Research Laboratories. I am immensely grateful to their support both during and after the experiments. They have been very willing to spend time in discussing the issues and aiding my understanding of the experiment.

Support throughout the data reduction period was provided by my advisor, Dr. Lyon B. King at Michigan Technological University. In addition to his monetary support, his keen insight into good scientific writing has aided me greatly in the preparation of this thesis. (Having said that, I should note that all shortcomings in this document are my own!)

I would also like to thank all those who provided helpful feedback on this thesis. Particular thanks go to my advisory committee: Dr. Gordon Parker, Dr. Song-Lin Yang, and Dr. Yoke Khin Yap. Dr. Dressler also provided insightful feedback and improved my understanding of atomic physics. Finally, my wife, Renata, waded through reams of paper in order to find and correct the numerous grammatical and typographic errors which spring up like weeds in my writing.

Funding for the research came from the Air Force Office of Scientific Research and from the Air Force Research Laboratories Space Scholars program.

Contents

List of Figures

List of Tables

Nomenclature

A	Cross-sectional area of the experiment volume, page 12
a, b, c, d	Cubit fit constants, page 32
A_{ij}	Einstein rate coefficient for spontaneous emission, page 6
B_{ij}	Einstein rate coefficient for stimulated emission, page 6
B_{ji}	Einstein rate coefficient for absorption, page 6
B_n	Background intensity data (counts), page 32
c	The speed of light in a vacuum, page 34
$\overline{E}$	Average energy, page 2
E	Beam energy (eV), page 20
e	Elementry charge, page 16
$E_{g_{max}}$	Maximum apparent beam energy on an RPA, page 21
f	Velocity or energy distribution function, page 6
f	View factor, page 13
$f(E)$	Energy distribution function (EDF), page 8
$f(v)$	Velocity distribution function, page 8
G	Geometric correction factor $(\text{Pa}^{-1}\text{m}^{-5})$, page 38
h	Planck's constant, page 34
I	Event rate (events/s), page 12
I	HET Current, page 3
I_b	Total beam current, $I_f + I_w$, (A), page 38
I_f	Beam current measured by the Faraday cup (A), page 38
I_n	Corrected spectrum $(\text{photons}/(\text{s m}^3))$, page 34

I_w Beam current measured by the collision cell wall (A), page 38

k A specific collisional process, page 6

k The Boltzmann constant, page 2

L Length of the experiment volume, page 12

$\dot{m}$ HET mass flow rate, page 3

m Particle mass, page 8

N Target particle number density, page 12

n Micrometer setting corresponding to spectrometer grating angle. Roughly the central wavelength of the spectrum acquired., page 27

n_e Electron number density, page 7

N_{events} The number of events that occur in an experiment, page 12

n_i First ion number density, page 3

n_i Number density of particles in state i, page 6

P Cell pressure $(\text{mtorr}, \text{Pa})$, page 38

P HET Power, page 3

P_λ Integrated peak height for transition at wavelength λ $(\text{photons}/(\text{sm}^3))$, page 36

q Beam particle charge number, page 16

Q_b Impacting beam number current $(\text{particles}/\text{s})$, page 12

R Ideal gas constant, page 38

R_n Raw intensity data (counts), page 32

s The sight line of a detector (m), page 8

s_d Detector electronic amplification $(\text{e}^-/\text{count})$, page 34

s_n Detector sensitivity function $(\text{photons}/(\text{e}^-\text{m}^3))$, page 34

T Maxwellian temperature, page 2

t Exposure time (s), page 34

t Viewing time, page 12

T_e Electron temperature, page 3

ΔV Maximum sag in RPA grid potential, page 20

v Particle velocity, page 8

V_{accel} HET acceleration voltage, page 3

$V_{g_{max}}$ Maximum apparent potential applied to an RPA that allows a beam of specific energy to pass, page 21

$\overrightarrow{v_k}$ Relative velocity between particles involved in collision process k, page 6

$V(x)$ The variance of quantity x, page 45

w Peak width at the baseline, page 30

W_T The Planck function for an object with temperature T (photons/(m^2s)), page 34

$W(x)$ Tungsten lamp intensity data (counts), page 34

x Detector pixel, page 32

$\epsilon_{\text{std}}(x)$ The standard deviation of quantity x, page 45

$\epsilon(x)$ The fractional error of a quantity x, page 45

λ Wavelength (nm), page 32

$\lambda(x)$ Pixel-to-wavelength mapping function (nm), page 32

σ Cross section, page 12

σ_λ Collision-induced emission cross-section for the transtion which emits at wavelength λ (cm^2), page 39

$\langle \sigma v \rangle$ Collisional rate coefficient, page 6

ξ_λ Relative cross section: $\xi_\lambda = G\sigma_\lambda$ ($\text{Pa}^{-1}\text{cm}^{-3}$), page 39

Chapter 1

Introduction

1.1 Overview

This thesis reports a series of experiments performed to determine ion impact emission cross sections for transitions of neutral xenon (Xe) when bombarded by singly- and doubly-ionized xenon (Xe^{+} and Xe^{2+}, respectively). Specifically, those transitions from the $5p^5 6p$ configuration into the $5p^5 6s$ configuration resulting in emissions in the near-infrared range from 700 nm to 1000 nm have been investigated. These experiments were conducted in the ion-luminescence apparatus of the Space Chemistry Laboratory in the Space Weather Center of Excellence of the Air Force Research Laboratory at Hanscom Air Force Base.

The data resulting from these experiments is of primary use in using the infrared emission lines of xenon as a diagnostic tool for determining the state of a xenon plasma. In particular, a diagnostic developed by Karabadzhak, Chiu, and Dressler[1] has been targeted. This diagnostic is designed for application on Hall effect thrusters, a particular class of electric spacecraft thruster.

After explaining the motivation of the research, the method of the experiment and the process by which the resulting data are analyzed are discussed. In Chapter 4 the data are presented. The thesis concludes with an example application of the cross section data and a discusion of these data's importance to the field of Hall effect thruster emission spectroscopy.

1.2 Motivation

1.2.1 Plasmas: their uses and fundamental features

Plasmas play an increasingly important role in modern technology. Plasmas of various types are used in electronics processing, heavy manufacturing, display technologies, and the aerospace industry. They are found in devices as common as the fluorescent lamp to less common devices such as spacecraft thrusters. In the aerospace industry, plasmas are most often associated with electric propulsion. There are several classes of electric thrusters which create plasmas and generate thrust typically by accelerating the

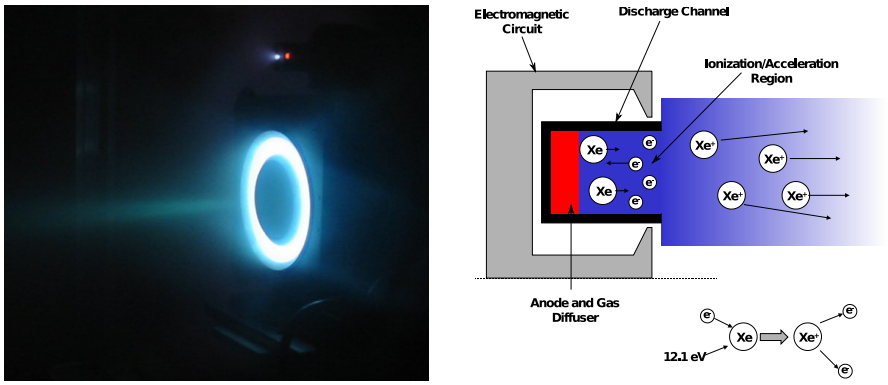

(a) A Hall effect thruster in operation

(b) Cross section of a HET chamber

Figure 1.1: A Hall effect thruster *(credit: Kieckhafer)*

heavy ions. Hall effect thrusters are one of the more common types of electric thrusters. The data developed in this thesis is particularly targeted at plasma diagnostics on these thrusters.

1.2.2 Hall effect thrusters

Hall effect thrusters (HETs) are a class of electric propulsion devices that use electric and magnetic fields to create a plasma and expel the ions at high velocity in order to generate thrust. Figure 1.1(b) shows a schematic diagram of a HET discharge chamber. Electrons from the cathode are trapped in a magnetic field near the mouth of the chamber. These electrons create an electric field between themselves and the anode, located in the back of the chamber. Electrons escaping the trap are accelerated into the anode and ionize the propellent, typically xenon, along the way. The propellent ions are accelerated in the opposite direction by the electric field, and then expelled, generating thrust.

Two critical parameters for understanding any plasma environment are the electron density, n_e and the electron temperature, T_e. The electron density is simply the number of free electrons present in a volume of space. Hall thruster plasmas are quasi-neutral—if n_i is the density of singly-charge ions, and there is a negligble density of multiply-charged ions, than $n_e \approx n_i$. Therefore, measurement of n_e directly provides a measure of n_i.

The electron temperature is usually defined as the Maxwellian temperature and is proportional to the mean kinetic energy of the electrons. In plasma physics it is customary to express temperature in units of energy, so:[2]

$$T_e(\text{eV}) = k\,[T_e(\text{K})] = 2\overline{E}. \tag{1.1}$$

Parameter	Symbol	Location	Value	Unit
Acceleration voltage	V_{accel}	N/A	300	V
Current	I	N/A	5.4	A
Mass flow	$\dot{m}$	N/A	63	sccm Xe
Power	P	N/A	1.6	kW
Electron temperature	T_e	Chamber	20-37	eV
		Plume	~ 3	eV
Ion number density	n_i	Chamber	0.20-2.0	$\times 10^{12}\text{cm}^{-3}$
		Plume	0.14-1.1	$\times 10^{12}\text{cm}^{-3}$

Table 1.1: Sample HET parameters

These parameters not only affect the way the plasma interacts with its mechanical environment, but also affect the way the plasma interacts with electric and magnetic fields. Ion densities are important for theroetical calculations HET thrust and efficiency. Electron temperatures and densities are important for understanding the ionization processes and mechanical erosion that occur in the discharge chamber. They are also important for understanding interactions between the thruster plume and the spacecraft, which can be potentially destructive to the craft. Consequently, the knowledge of these parameters is of vital importance for designing and controlling devices which make use of plasmas.

Thruster operating parameters, such as acceleration voltage, current, and mass flow vary depending on the thruster and the desired performance. The plasma parameters are dependent on the thrusters operating parameters at its geometrical and magnetic configuration. Sample operating and plasma paramters in the discharge chamber and plume of a hall thruster are listed in Table 1.1.[3]

1.2.3 Optical emission spectroscopy on plasmas

Optical emission spectroscopy (OES) is an attractive diagnostic in electric propulsion, as well as other fields. Theoretically, one can use it to determine both electron temperature and electron number density[4,5,6,7] and it may be possible to determine non-Maxwellian electron energy distribution functions.[8] Because OES is entirely passive and non-invasive, it guarantees that the plasma is not disturbed in the process of taking the measurement. Furthermore, it is possible to use OES in regions of plasma that are inaccessible, either because they are hostile to physical probes or because they are physically remote. An example of the latter is a thruster in operation on a satellite in orbit.

1.2.4 Atomic radiation

Before exploring OES, a basic understanding of atomic radiation—the processes that result in optical emission from plasma—is necessary. Though we are using OES to measure properties of the free electrons in the plasma, the electrons themselves do not

emit the radiation that is studied. Rather, interactions between the electrons and the atoms and ions cause these heavy particles to emit.

Atoms and ions may be described by their *configuration*. The configuration describes the orbitals of all of the electrons bound to the atom or ion. Each configuration is associated with a quantized energy level. The electrons normally reside in the ground-state configuration in which the electrons occupy the lowest energy levels available to them. The atom may become excited—that is, the system may gain more energy—through collisions with other particles, or by the absorption of photons. When this happens, one or more electrons are raised from the ground state to higher energy levels. An atom in an excited configuration eventually decays back to the ground state, either directly or through intermediate energy levels, releasing the energy lost as one photon per level transition. The energy lost by the atom is contained in the photon, and is related to the photon's wavelength by $E = hc/\lambda$. This is the process of *spontaneous emission*, and the resulting photons comprise the emissions that are studied with OES. Since each transition has a unique energy difference, the transition that occurred may be identified by the wavelength of light emitted.

The atom resides in the higher energy configuration for a finite amount of time. The exact amount of time is subject to quantum fluctuations, but a statistical weight may be assigned that describes the average rate at which transitions from a given energy level to another. This weight is known as the *Einstein coefficient* for spontaneous emission and is denoted by the symbol A_{ij}.[9]

In addition to spontaneous emission, two other processes occur. The first is *absorption*. When a photon of an energy that corresponds to a particular upward transition is incident on an atom with an electron residing in the lower state of that transition, the atom will absorb the photon and the electron will undergo the transition into the upper level. The reverse of this process is *stimulated emission*. When a photon of an energy that corresponds to a downward transition available to an electron in an excited state is incident on the atom, the photon may stimulate the electron to that downward transition resulting in two photons as the electron transitions to the lower state. The rates of these processes for a given transition are governed by the Einstein coefficients for absorption and stimulated emission, B_{ji} and B_{ij}, respectively.

While it is intuitive to think of a single electron moving from state to state, there is considerable coupling between the electrons in large atoms. Therefore it is more appropriate to speak of excited configurations. Here the configuration notation itself is conceptually misleading since it implies that exactly one electron is excited, while the others remain in their previous states. The reader is advised to bear this in mind.

The transitions with which this thesis deals are from the $5p^5 6p$ configuration of the xenon atom decaying into the $5p^5 6s$ configuration. There are ten such $5p^5 6p$ levels, and four $5p^5 6s$ levels, each numbered in decreasing order of energy (see Appendix A). Figure 1.2 shows the energy level diagram with the ten 6p levels. The transitions investigated in this thesis are marked on the figure. In addition to the standard configuration notation, spectrographic Paschen notation is also used throughout this thesis. In Paschen notation, the $5p^5 6p$ configuration is denoted "2p" and the $5p^5 6s$ configuration is "1s." The ten different levels may be denoted in this notation as $2p_1$ through $2p_{10}$, with $2p_1$ having the highest energy.

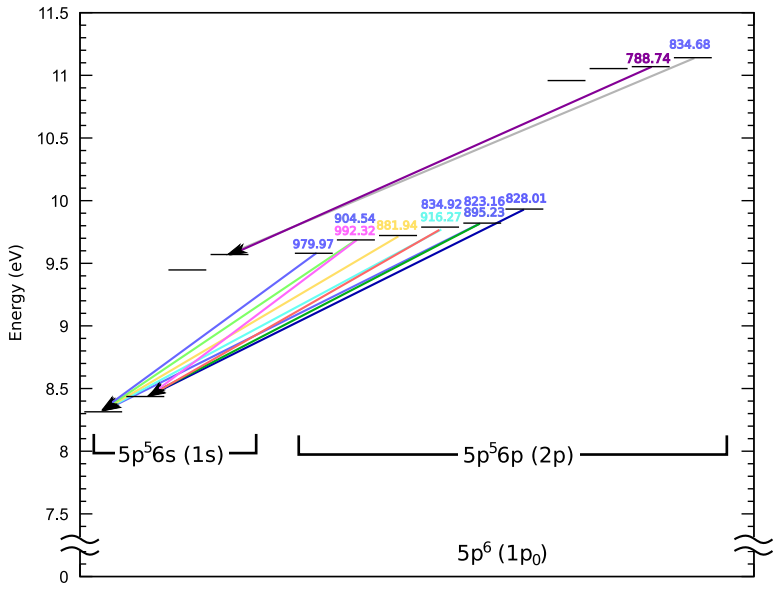

Figure 1.2: The energy level diagram of the transitions of xenon studied in this thesis. The transition wavelength in nanometers are printed on the chart.

1.2.5 From plasma emissions to plasma parameters

In order to measure the plasma parameters using the OES method three things are needed:

- The emission spectra in photons per unit time
- A model relating the plasma parameters to the emission spectra
- Accurate cross section data for the processes in the model

Numerous models are available in the literature, and it is up to the owner of a plasma to acquire the spectra. However, the availability of cross section data is often the weak link. Cross sections for some elements, such as hydrogen, have been extensively studied,[10,11,12,13] others, such as xenon are just now being studied in greater detail. Thus, if one is in the field of electric propulsion, where many of the plasmas created are xenon, the application of spectroscopic methods may be infeasible without first measuring important cross sections. To understand why the cross sections are important, it is helpful to look at how a spectroscopic diagnostic works. Most spectroscopic models begin with a detailed balance of the processes taking place in the plasma. These processes are:[14]

1. Radiative
   (a) Radiative transitions in atoms and ions

(b) Free-bound transitions: electron-ion recombination, and its reverse, photo-ionization

2. Collisional

   (a) Electron impact excitation and de-excitation of atoms and ions

   (b) Ion and neutral impact excitation and de-excitation of the atoms and ions

   (c) Impact (electron, ion, or neutral) ionization and its reverse, three body recombination

   (d) Autoionization and dielectronic recombination

As discussed in Section 1.2.4, the Einstein coefficients describe the rates at which transitions occur between two states, i and j. For collisional processes, k, the rate coefficient,

$$\langle \sigma_{k_{ij}} v_k \rangle = \frac{\int \sigma_{k_{ij}} v_k f(\overrightarrow{v_k}) d^3\overrightarrow{v_k}}{\int f(\overrightarrow{v_k}) d^3\overrightarrow{v_k}} \tag{1.2}$$

describes the rate at which the process k excites an atom or ion from state i to state j. Here $f(\overrightarrow{v_k})$ is the relative velocity distribution function for the species involved in process k. For isotropic processes this may be converted to $f(E_k)$, the energy distribution function (EDF), through a change in the independent variable according to $E = \frac{1}{2}mv^2$.

Using these rates, a system of equations can be derived which describes all of the processes that occur. For the fraction of a radiative species in state i at steady state, the rate of transitions out of state i to other states j must be equal to the rate of transitions into state i:

$$\overbrace{\sum_{j \neq i} n_i \left[\underbrace{A_{ij}}_{\substack{\text{spontaneous emission} \\ (i > j)}} + \underbrace{B_{ij}\rho\left(\nu_{ij}\right)}_{\substack{\text{stimulated emission } (i > j) \\ \text{absorption } (j > i)}} + \underbrace{\sum_k n_k \langle \sigma_{k_{ij}} v_k \rangle}_{\substack{\text{collision-induced} \\ \text{excitation/de-excitation}}} \right]}^{\text{Transitions out of state } i \text{ to all other states } j}$$

$$= \underbrace{\sum_{j \neq i} n_j \left[A_{ji} + B_{ji}\rho\left(\nu_{ij}\right) + \sum_k n_k \langle \sigma_{k_{ji}} v_k \rangle \right]}_{\text{Transitions from all other states } j \text{ into state } i} \tag{1.3}$$

The left side of the equation accounts for the rate of transitions from state i to all other states j, while the term on the right accounts for the rate of all transitions from other states into state i. To be complete, the states i and j may include transitions to and from continuum regions, such as free electron states. It should be noted that for continuum regions the summations should properly be replaced with integrals. Within each outer summation, the first term accounts for spontaneous emission, the second term accounts for either stimulated emission or absorption, depending on whether state i is of greater or lesser energy than j, and the third term accounts for all collisional processes, k.

Equation 1.3 must hold for every state i in the system. Together such equations for every state i comprise a system of equations, that if solved simultaneously, completely describe the radiative processes, and therefore have predictive power. Because this system of equations is effectively infinite, simplifications must be made so that only the dominate processes are included in the model. In nearly all cases the higher energy transitions are neglected as they are typically small contributions.[15] This has the advantage of removing the continuum regions from the system of equations, since transitions into the continuum regions are typically high energy.

As a pedagological example, consider the coronal equilibrium model, so-called because of its applicability to the conditions in the corona of the sun. The first simplifying assumption is that emissions resulting from collisions between heavy particles (neutrals and ions) are negligible because these collision rates are low. Therefore, the only collisional process considered are collisions between electrons and heavy particles. Thus, in Equation 1.3 $k \rightarrow e$ and the summations over k are removed. Secondly, it is assumed that all upward transitions result from collisional excitation because the radiation density is low. Furthermore, all downward transitions are assumed to be radiative, because electron density is low and the collision rate coefficient is also low. To be more precise, for $j > i$:

$$n_j A_{ji} \gg n_e n_j \langle \sigma_{e_{ji}} v_e \rangle \tag{1.4}$$

and

$$n_e n_i \langle \sigma_{e_{ij}} v_e \rangle \gg n_i A_{ij} \tag{1.5}$$

It is assumed that the plasma is optically thin, so that most of the photons escape without being reabsorbed,

$$n_i B_{ij} \approx 0 \tag{1.6}$$

$$n_j B_{ji} \approx 0. \tag{1.7}$$

Inserting these assumptions into Equation 1.3 yields for each state i:

$$\sum_{j>i} n_i n_e \langle \sigma_{e_{ij}} v_e \rangle + \sum_{j<i} n_i A_{ij} = \sum_{j>i} n_j A_{ji} + \sum_{j<i} n_j n_e \langle \sigma_{e_{ji}} v_e \rangle \tag{1.8}$$

If we assume that the ground state population is much larger than any of the excited states, and therefore upward transitions from the ground state dominate, then we may reduce Equation 1.8 for each excited state i to

$$n_i \sum_{j<i} A_{ij} = n_0 n_e \langle \sigma_{e_{0i}} v_e \rangle. \tag{1.9}$$

For N_i particles in state i, the fraction of them that will transit to state r and give rise to radiation $\rho(\nu_{ir})$ is

$$\frac{N_{i \rightarrow r}}{N_i} = \frac{A_{ir}}{\sum_{j<i} A_{ij}}. \tag{1.10}$$

Multiplying this into both sides of Equation 1.9, the intensity of radiation collected by a detector is

$$I(\nu_{ir}) = \frac{1}{4\pi}\int n_i A_{ir} ds = \frac{1}{4\pi}\int n_e n_0 \langle \sigma_{e_{0i}} v_e \rangle \frac{A_{ir}}{\sum_{j<i} A_{ij}} ds \tag{1.11}$$

where the line integral is along the line of sight, s, of the detector. This equation may be used to calculate emissive output of a plasma given species densities and an EEDF.

Typically, the reverse of this process is desired. That is, one knows the intensities of various lines, and would like to determine the electron temperature or density. To accomplish this, ratios of line intensities can be used to eliminate the electron density from Equation 1.9. For two transitions a and b in the same species—that is with a common ground state—each originating in their own i level and transitioning to their own r level:

$$\frac{n_{a_i}}{n_{b_i}} = \frac{n_0 n_e \langle \sigma_{a_{0i}} v_a \rangle / \sum_{j<i} A_{a_{ij}}}{n_0 n_e \langle \sigma_{b_{0i}} v_b \rangle / \sum_{j<i} A_{b_{ij}}} \tag{1.12}$$

$$= \frac{\langle \sigma_{a_{0i}} v_a \rangle \sum_{j<i} A_{b_{ij}}}{\langle \sigma_{b_{0i}} v_b \rangle \sum_{j<i} A_{a_{ij}}}. \tag{1.13}$$

Following the same logic used from Equations 1.9 to 1.11, the ratio of line intensities may be written:

$$\frac{I(\nu_{a_{ir}})}{I(\nu_{b_{ir}})} = \int \frac{\langle \sigma_{a_{0i}} v_a \rangle}{\langle \sigma_{b_{0i}} v_b \rangle} \frac{A_{a_{ir}}}{A_{b_{ir}}} \frac{\sum_{j<i} A_{b_{ij}}}{\sum_{j<i} A_{a_{ij}}} ds. \tag{1.14}$$

Typically some integral inversion, such as the Abel inversion,[16] is used to extract point ratios from the line-integrated ratios, yielding:

$$\frac{\rho(\nu_{a_{ir}})}{\rho(\nu_{b_{ir}})} = \frac{\langle \sigma_{a_{0i}} v_a \rangle}{\langle \sigma_{b_{0i}} v_b \rangle} \frac{A_{a_{ir}}}{A_{b_{ir}}} \frac{\sum_{j<i} A_{b_{ij}}}{\sum_{j<i} A_{a_{ij}}}. \tag{1.15}$$

At this point, it is usually necessary to assume an EEDF in order to proceed futher. Often a Maxwellian distribution is assumed such that:[17]

$$f(v) = \left(\frac{m}{2\pi kT}\right)^{3/2} \exp\left(-\frac{mv^2}{2kT}\right) \tag{1.16}$$

Therefore, substituting this into Equation 1.2 the rate coefficient may be expressed as:

$$\langle \sigma_{_{ij}} v \rangle = 4\pi \left(\frac{m}{2\pi kT}\right)^{3/2} \int_0^\infty \sigma_{ij}(v) v^2 \exp\left(-\frac{mv^2}{2kT}\right) dv. \tag{1.17}$$

Using the kinetic energy, $E = \frac{1}{2}mv^2$, this may be rewritten in terms of energy as

$$\langle \sigma_{ij} v \rangle = \frac{2m}{\sqrt{\pi}(kT)^{3/2}} \int_0^\infty \sigma_{ij}(E)\sqrt{E} \exp\left(-\frac{E}{kT}\right) dE. \tag{1.18}$$

The preceding reformulation is important because cross section values are typically given in terms of energy, rather than velocity. Finally, one substitutes Equation 1.18 into Equation 1.15 yielding,

$$\frac{\rho(\nu_{a_{ir}})}{\rho(\nu_{b_{ir}})} = \frac{\int_0^\infty \sigma_{a_{0i}}(E)\sqrt{E}\exp\left(\frac{E}{kT}\right) dE}{\int_0^\infty \sigma_{b_{0i}}(E)\sqrt{E}\exp\left(\frac{E}{kT}\right) dE} \frac{A_{a_{ir}}}{A_{b_{ir}}} \frac{\sum_{j<i} A_{b_{ij}}}{\sum_{j<i} A_{a_{ij}}}. \tag{1.19}$$

To apply Equation 1.19, the cross section data, usually in the form of an empirical fit to measured data must be provided. With these data, the electron temperature may be found, usually through iterative calculation. Although Equation 1.18 is integrated over all energies from $E = 0$ to $E = \infty$, it is typically only necessary to have cross section data available for energies in the range of

$$1 < \frac{E}{kT} < 10 \tag{1.20}$$

as the square root dependency on E limits the contributions to the integral on the low end, and the exponential dependence on $-E$ limits the contributions from the high end.[15] This important approximation enables the model to function so long as a limited set of cross section data are available in the appropriate energy range for a particular plasma. Unfortunately, reliable cross section data for heavy atoms is largely unavailable.

The corona model is, perhaps, the simplest model, owing to the large number of assumptions that are made in order to reduce the set of Equations 1.3 to a managable size. It requires only electron impact excitation cross section data for the plasma neutral species in order to implement it. For more complex models, more cross sections are required. For any given model, cross section data for every collisional process incorporated must be available for that model to have predictive or analytical value.

To improve the accuracy of the corona model, a class of models, collectively called collisional-radiative (CR) models, were first developed by Bates, et al.[18] The fundamental extension over the corona model is that electron collisions causing transitions between excited states are taken into account. This enables CR models to account for stepwise excitation to higher levels which improves the accuracy of the model. These models are particularly effective in plasmas with higher electron densities and temperatures where the mean time between collisions is smaller.

1.2.6 Application of OES to Hall effect thrusters

Several attempts have been made to use the corona model on Hall thrusters. Pagnon, et al. used the corona model in conjunction with actinometry in studying the erosion products of a HET.[19] Their results show that it is possible to measure the absolute rate of erosion products given an appropriate calibration. However, they do not attempt to

measure either electron temperature or density using OES, and rather rely on electrostatic probes for these data. Karabadzhak, Semenkin, and Manzella attempted to use the corona model to determine these properties, but concluded that the model did not provide sufficiently accurate data.[20] These experiments led to the development of a more complex model which will be discussed shortly.

More complicated models exist. For instance, Leray, Bonnet, and Pigache adapted a CR model originally developed for argon by Guimarães[21,22] for application to Hall thrusters.[23] In order to access the higher energy portion of the electron energy distribution function (EEDF) Guimarães introduced helium into the thruster gas and compared the emissions from the helium as well as xenon. He found that mixtures of up to 10% of helium did not affect thruster operation, and enabled them to make preliminary estimations of electron density, ionization degree and the shape of the EEDF.

The model developed by Karabadzhak, Chiu, and Dressler may be the most complete model in use at this time. It incorporates the following processes:[1]

$$\mathrm{e}^- + \mathrm{Xe} \longrightarrow \mathrm{Xe}^* + \mathrm{e}^- \tag{1.21}$$
$$\longrightarrow \mathrm{Xe}^{n+*} + (n+1)\mathrm{e}^- \tag{1.22}$$
$$\mathrm{e}^- + \mathrm{Xe}^+ \longrightarrow \mathrm{Xe}^{n+*} + n e^- \tag{1.23}$$
$$\mathrm{e}^- + \mathrm{Xe}^m \longrightarrow \mathrm{Xe}^* + \mathrm{e}^- \tag{1.24}$$
$$\longrightarrow \mathrm{Xe}^{n+*} + (n+1)\mathrm{e}^- \tag{1.25}$$
$$\mathrm{Xe}^+ + \mathrm{Xe} \longrightarrow \mathrm{Xe}^{+*} + \mathrm{Xe}^* \tag{1.26}$$
$$\mathrm{Xe}^{2+} + \mathrm{Xe} \longrightarrow \mathrm{Xe}^{2+*} + \mathrm{Xe}^* \tag{1.27}$$
$$\longrightarrow \mathrm{Xe}^{+*} + \mathrm{Xe}^{+*} \tag{1.28}$$

where the 'm" superscript indicates a metastable state, and the "*" superscript indicates an excited state.

One of the key features of this model is that it incorporates not only electron collision excitation processes (Equations 1.21 to 1.25), but it also incorporates ion collision excitation processes (Equations 1.26 to 1.28). Collision cross sections typically scale with particle velocity. An ion with a specific velocity will have roughly the same cross section for emission as an electron with the same velocity. In coronal plasmas, the ion temperatures are no greater than the electron temperature, and usually much smaller. Since ions are much more massive than the electrons, this corresponds to ion velocities that are typically three orders of magnitude smaller than the electron velocities. Under these conditions, the cross sections for electron impact excitation are much higher than those for ion collision excitation. This is the justification for ignoring the ion collision processes in the corona model and in most CR models. In a Hall thruster the ions are accelerated to a typical energy of 300 eV where the cross sections are comparable to the cross sections for the electron impact excitation at typical temperatures ~ 10 eV.[24]

1.2.7 The need for xenon cross section data

Nearly all the authors who have attempted to use optical emission spectroscopy have noted the lack of complete cross section data. Without these data, the researchers

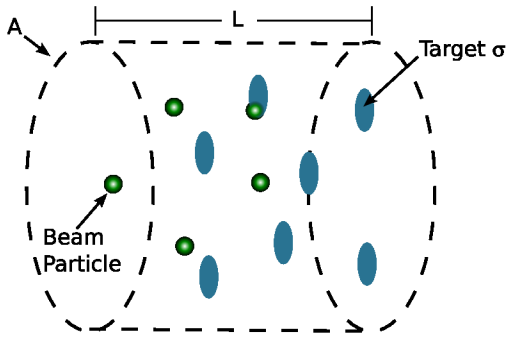

Figure 1.3: Basic cross-section derivation

are forced to estimate the cross sections based on theoretical approximations such as the Born approximation, which are not appropriate for atoms as complicated as xenon. In recent years theorists have used more sophisticated models to better calculate some xenon cross Sections.[25,26] This work has been of great help to experimentalists working on HET OES. However, these theoretical cross sections are still subject to errors on the order of a factor of two.[24]

Fueled by these needs, experimentalists are beginning to measure xenon cross sections. Fons and Lin presented a widely cited work that provides electron collision excitation cross sections (corresponding to Process 1.21) for transitions from the $5p^5 6s$ configuration of xeneon to the $5p^5 6p$ configuration.[27] Futher studies by the group have yielded cross section data for the transitions from $5p^5 6s$ (J=2) metastable state.[28] When combined with branching ratios (the fraction of transitions from a higher state that go to a particular lower state) these yield emission cross sections.

Models such as Karabadzhak's require not only electron impact emission cross sections but ion impact emission cross sections as well. At the time of this publication, the author is only aware of one prior study, which experimentally investigated any of the ion impact excitation cross sections of xenon,[24] and it only investigated them at one energy level. The work in this thesis extends the available xenon ion impact emission cross section data.

1.3 Overview of cross sections

Having established the importance of impact emission cross sections, a brief explanation of their physical derivation is warranted. A cross section is a way of expressing the probability of an event occuring at a particular set of conditions. Loosly speaking, a cross section for an event describes how big of a target a particle is. This is explained graphically in Figure 1.3. Q_b beam particles per second pass through area A. Within the volume $V = AL$ lie N target particles each with cross-sectional area σ. Assuming the density of the targets is low enough so that one target does not occlude another as

seen from the direction of beam travel,* the probability that a beam particle will hit a target is given by $N\sigma/A$. If one observes the volume for a time t, the expected number of times a beam particle will interact with a target and cause the event is

$$N_{\text{events}} = \frac{N\sigma}{A} Q_b t, \tag{1.29}$$

which can be rearranged to yield

$$\sigma = \frac{N_{\text{events}} A}{Q_b N t}. \tag{1.30}$$

Defining $I = N_{events}/t$, the rate at which events are witnessed, and using the target particle number density, $n = N/V$, we can rewrite Equation 1.30 as

$$\sigma = \frac{I}{L Q_b n}. \tag{1.31}$$

For impact induced emission cross sections, "witnessing" the events means measuring the intentisy of the radiation that results from the excitation and subsequent relaxation of an atom or ion after a particle collision occurs.

Radiation trapping is one of the main difficulties in many experiments designed to measure cross sections. Radiation trapping may occur when the radiation emitted by the event under study is reabsorbed by other atoms or ions within the volume under study. If the radiation is reemitted at the same wavelength, then it may be treated as if it were never absorbed in the first place, and radiation trapping is not considered to have occurred. However, it may be the case that the energy absorbed by the atom from the radiation is reemitted at a different wavelength, or in diffent modes altogether (e.g. collisionally). In this case, the radiation is lost to the experiment.

Radiation trapping manifests itself as a dependency of the emissions on the pressure of the target gas. The nature of the pressure dependency depends on the configuration of the atoms under study. While absorbtion of the target radiation and re-emission at other wavelenths may account for an apparent decrease in the cross section, an "artificial" population of the upper level through cascade transtions from still higher levels may show an apparent increase in the cross section.

*This assumption is not necessary for accurate calculation of cross-sections because absolute cross-sections are defined based on single collisions. However, the explanation given is closer to the setup of the experiments on which this thesis reports, and any corrections necessary for occlusions of targets are handled by scaling of relative data to known absolute cross-sections.

Chapter 2

Experiment

2.1 Overview

An experimental setup has been devised in order to accurately measure the emission cross sections resulting from atomic collisions. The general setup of this type of experiment is described in the literature by Lin's group at the University of Wisconsin.[29] A charged particle (electron or ion) beam of known current is directed into a stationary target gas at a specific number density. The resulting emissions are viewed with a spectrograph, and the intensity of the transitions of interest are measured.

The method of the experiment is derived from the basic picture of the cross section given in Figure 1.3. Given a charged particle beam, it is simple to measure the beam current in particles per second, Q_b, by measuring the electric current of the beam as it impacts a metal target. The number density of targets may be calculated via pressure measurements and the appropriate use of an equation of state. However, the absolute emission, I, intensity, and the path length, L, are more difficult. The intensity recorded by the detector is an unknown fraction, f, of the absolute emission; the remainder of the photons are emitted in the wrong direction to be directly viewed by the detector. Some of these may eventually be reflected into the detector, but others are absorbed by the walls or other objects and lost to the experiment. This absorption is dependent on the view factor and chamber materials. However, it is constant from experiment to experiment provided that the geometry and materials do not change. Likewise, the path length L is not a simple constant, but a function of the view that the detector has of the volume in which collisions occur. As with f, this factor is dependent only on experimental geometry.

In these experiments, no attempt is made to explicitly determine f or L. Rather, the measured cross sections are assumed to contain an unknown "geometric factor," G which accounts for the unknowns. Determination of the geometric factor is done by comparing the results of the portion of these experiments which overlap with previously published data. This process is discuessed in greater detail in Section 3.3.

A schematic of the experiment is shown in Figure 2.1. Xenon ions are generated using a DC arc discharge. The ions are accelerated to the desired energy through a potential drop between the discharge chamber and the collision cell. Along the way

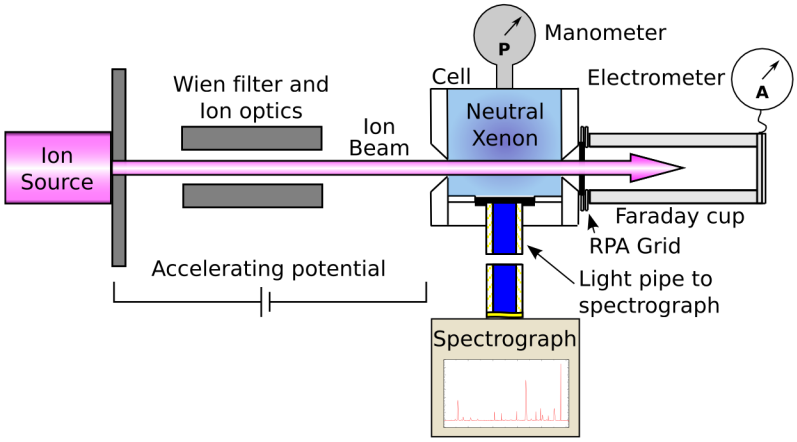

Figure 2.1: Schematic representation of the ion excitation cross-section experiment

they are selected for the desired mass and charge by a Wien velocity filter. A system of electrostatic lenses focuses the beam into the collision cell, assuring minimal beam divergence. The collision cell is an aluminum cube which is electrically isolated. A beam entrance aperature is drilled in the front side of the chamber, and an equal aperature is opposite it on the back side. A retarding potential analyzer (RPA) is placed behind the exit aperature and is used to measure the beam energy. The back wall of the chamber is electrically isolated from the remainder of the chamber and collects current in order to monitor the beam divergence. Currents on the RPA collector and on the chamber backplate are measured with computer-controlled electrometers. On one side of the chamber a capacitance manometer is attached. Opposite the manometer is an entrance for the target gas. On a third side wall a fiber optic views the chamber, collects the light emitted from the collisions, and transfers it to the spectrograph located outside of the vacuum chamber.

2.2 Equipment

2.2.1 Ion beam

The ion source for this experiment is a commercial system developed by Colutron Research Corporation. A diagram of the source is shown in Figure 2.2 It creates a discharge plasma between a hot filament and a metal anode within a quartz cylinder approximately 2.5 cm in diameter and 5 cm tall. The anode also acts as the top of the cylinder. The source is designed to be used with any desired gas. In order to create a xenon ion beam, the filament is held between 20 and 30 V below the anode so that electrons emitted from the filament gain sufficient energy to create singly- and doubly-ionized xenon. A pin-hole in the center of the anode allows some of the ions to escape

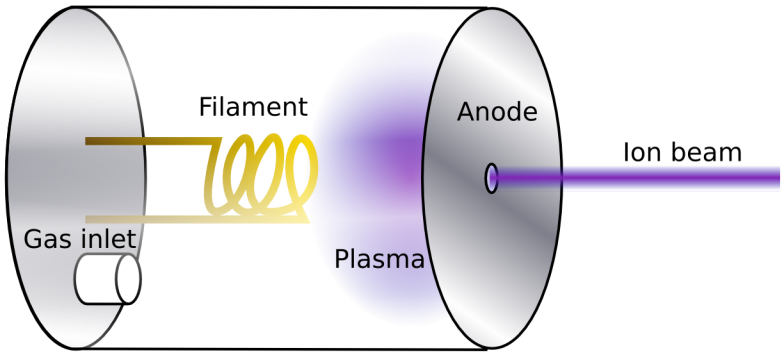

Figure 2.2: Schematic representation of the ion source

the discharge chamber and form a beam.

Once the ions have escaped the discharge chamber, they are accelerated by the potential drop between the anode and the collision cell, which is at ground. The beam path extends approximately 1 m, through a Wien filter and several electrostatic lenses. The Wien filter selects only those particles with the desired mass-charge ratio—that is, only those particles with the desired ionization stage. The electrostatic lenses focus the beam to a narrow width, compensating for the beam's natural tendency to diverge due to the constituent particles' mutual repulsion. The lenses are all driven by Kepco PCX-100 or PCX-200 rack-mount power supplies.

Wien velocity filter

The Wien filter is of particular import, and it is vital that it be appropriately adjusted to ensure that the beam is comprised of the correct ions. The ion source itself is rather indiscriminate; electrons emitted from the filament may create not only multiple ionization levels of the source gas (xenon, in the case of these experiments) but also may ionize any trace elements present in the discharge chamber. These may include nitrogen, oxygen, and other atmospheric elements not fully evacuated, or erosion products of tunsgsten and steel constituents. Due to the relatively low quantaties of these elements, a beam of their ions will typically be small in current, but it may still be possible to detect them using a electrometer of sufficient resolution. Therefore, the procedure for tuning the Wien filter must ensure that the desired species has been selected. This was done by finding one or more secondary species in the correct spot relative to the desired species.

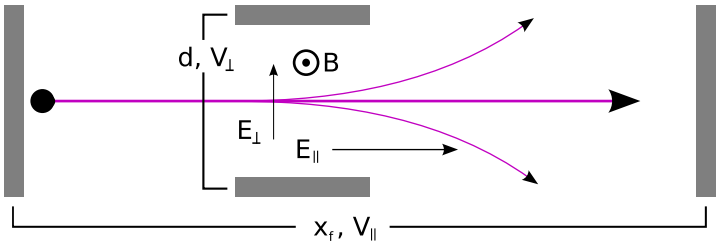

Figure 2.3: Schematic representation of a Wien velocity filter

The Wien filter is a short region of space through which the charged particles pass (see Figure 2.3). In this region, an electric and a magnetic field are applied perpendicular both to each other and to the intended beam trajectory. At the end of this region, an aperature blocks any particle that does not travel straight through the filter. The magnitude of the electric and magnetic fields are set so that for particles with the desired mass-to-charge ratio the forces resulting from the fields exactly balance. In our configuration the Wien filter is locatated at position x, partway through a region in which the ions of mass m and charge qe are accelerated by an applied field, $E_{\|} = V_{\|}/x_f$, where "$\|$" denotes "parallel to the beam path." The voltage at the location of the Wien filter is therefore:

$$V_{\|}\frac{x}{x_f}. \tag{2.1}$$

The particles velocity upon reaching the Wien filter, assuming it started at rest, is then given by:

$$v = \sqrt{2mE} = \sqrt{2eV_{\|}\frac{x}{x_f}\frac{q}{m}}. \tag{2.2}$$

Assuming that the filter is sufficiently short so that the parallel velocity changes little during the time that the particle passes through the field we may then determine which particles will pass through the filter, and which will be deflected. Only those particles for which the force induced by the magnetic field balances the force induced by the electric field will pass undeflected. Mathematically,

$$\overrightarrow{F_E} = -\overrightarrow{F_B} \tag{2.3}$$

$$qe\overrightarrow{E_{\perp}} = -qe\overrightarrow{v} \times \overrightarrow{B} \tag{2.4}$$

$$qe\frac{V_{\perp}}{d} = qeB\sqrt{2e\frac{V_{\|}}{x_f}\frac{q}{m}} \tag{2.5}$$

$$V_{\perp} = Bd\sqrt{2e\frac{V_{\|}}{x_f}\frac{q}{m}}. \tag{2.6}$$

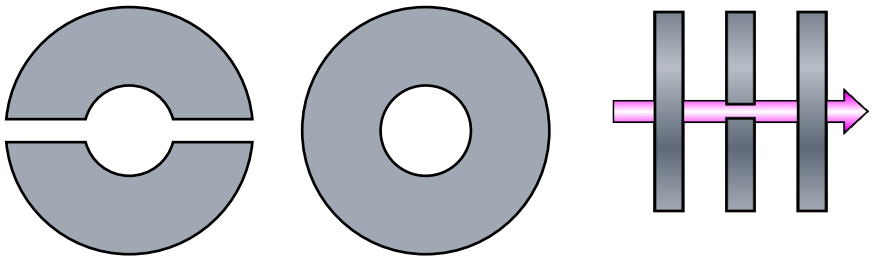

(a) A steering ion optic

(b) A collimating ion optic

(c) A system of ion optics

Figure 2.4: Diagrams of ion optics

Comparing the Wien filter voltage necessary to select a particle with charge-to-mass ratio q_1/m_1 to the voltage necessary to select a second particle with ratio q_2/m_2 we see

$$\frac{V_{\perp_2}}{V_{\perp_1}} = \sqrt{\frac{q_2/m_2}{q_1/m_1}}, \tag{2.7}$$

assuming the dimensions, acceleration voltage and magnetic field are held constant.

Making use of Equation 2.7 we devised the following procedure for tuning the filter:

1. Set the desired acceleration energy and an arbitrary magnetic field
2. Scan the Wien filter voltage until a peak in the beam current is found
3. Make an educated guess as to which species has been found
4. Supposing the guess to be correct, chose another species expected to be present in the source and calculate using Equation 2.7 at what filter voltage it should be found
5. Check that the second species is actully found at the new filter voltage

Steps 4 through 5 may be repeated for as many species as are expected to be present until one is sufficiently confident in the guess of the original species. Naturally, if other species are not found at the calculated positions, one must go back to Step 3 and try again.

Ion optics

The ion optics in the experiment come in two types: steering and collimating. The steering lenses are two semicicular metal plates with a hole between them (Figure 2.4(a)).

By applying differing voltages the ion beam may be steered vertically, as in the configuration in the figure, or horizontally if the optic is rotated by 90 degrees.

The collimating optics are full metal discs with a hole through which the beam passes (Figure 2.4(b)). If the potential set on the lens is less than the potential of the beam as it approaches it, the beam tends to converge on entry to the lens, and diverge on exit. If the potential is higher, the opposite is true. Because the goal is to have the beam converge, the competing upstream and downstream effects of the lens are difficult to handle. Multiple lenses are used so that the later lenses can mitigate the problems caused by earlier lenses without degrading convergence (Figure 2.4(c)). While one could simulate the beam path using software such as Simion and thereby arrive at optimal settings for the lenses, it was sufficient for our purposes to achieve convergence through repeated adjustments to the lenses.

2.2.2 Electron beam

The electron source used in these experiments is a simple tungsten filament followed by four electrostatic lenses. The filament is driven by a Kepco PCX-100 supply. Current passing through the filament excites some electrons to be emitted from the material. Emitted electrons are accelerated by a potential difference between the filament and the lenses. The entire source is approximately 30 mm deep by 10 mm tall by 40 mm wide. The electron source is mounted in the main vacuum chamber approximately 150 mm from the collision cell.

2.2.3 Collision cell

The collision cell is an aluminum cube 25 mm on each side. On the front side, a hole allows the charged particle beam to enter the chamber. It passes through the collision cell and through a hole on the back side into the Faraday cup (see Section 2.2.6). The back wall of the chamber is electrically isolated from the rest of the chamber so that any divergent portion of the beam may be collected and measured. An optical fiber is connected to the bottom of the chamber which allows emissions to be collected and passed to the spectrograph. The gas feed is connected to one side of the chamber to pressurize the chamber with the target gas. An MKS capacitance manometer model 690A01TRC is connected to the other sides and monitors the chamber pressure.

2.2.4 Spectrograph

The spectrograph used was a Thermo Jarrell Ash model 82-479 which is a 0.156 m (F/3.7) Czerny-Turner design. All experiments used a 1200 lines-per-inch diffraction grating with a blaze at 600 nm and a 50 μm entrance slit. An Andor iDus DU420A-OE electrically cooled CCD detector with 1024 horizontal pixels was used to record the spectra. In this configuration the spectrograph could resolve wavelength differences of approximately 0.2 nm over the range of interest.

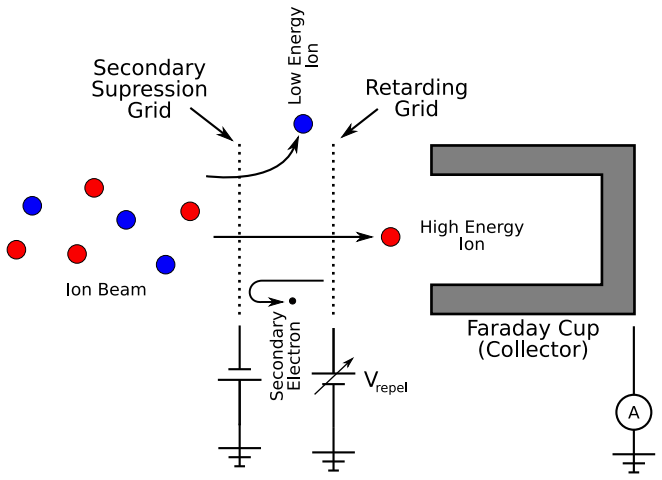

Figure 2.5: Schematic represenation of an RPA

2.2.5 Calibration

Two windows are mounted on the vacuum chamber. Attached to one of the windows is a mercury lamp which may be used for wavelength calibration of the spectrograph. A halogen-tungsten lamp is attached outside the second window and is used to determine the spectral sensitivity of the spectrograph. The temperature of the halogen-tungsten lamp has been measured with a pyrometer and is 3065 K. To the extent possible, the chamber and equipment outside is covered with black cloth to prevent ambient light from leaking in.

2.2.6 Retarding potential analyzer

A retarding potential analyzer (RPA) is placed outside of the collision cell to collect and monitor the beam energy. An RPA is an electrostatic device for measuring the energy distribution function (EDF) of the incident particles. The basic design consists of a metal grid whose voltage may be swept to deflect (retard) particles of "low" energies and prevent them from reaching the detector placed behind it.[30] Figure 2.5 depicts the RPA used in these experiments. For an RPA designed to measure the ion EDF, the retarding grid is swept from plasma potential to more postive potentials until no current is detected on the plate. At plasma potential, all ions are collected by the detector, and as the retarding potential is raised the lower energy ions are deflected away from the detector. The EDF, $f(E)$, is therefore proportional to

$$f(E) \propto -\frac{1}{q}\frac{dI(E)}{dV}. \tag{2.8}$$

The exact EDF may be determined from this equation by normalizing its area to one:

$$\int_0^\infty f(E)dE = 1. \tag{2.9}$$

Since the energy of an incident particle is directly related to the voltage on the detector by $E = qeV$ we can change the independent variable in Equation 2.8 from E to V, where V is the voltage of the detector plate—the parameter under experimental control.

While the RPA is a simple device, it does suffer from two major problems. The first is the release of secondary electrons by the impact of the ions into the detector surface or the repeller grid. In particular, secondary electrons from the grid will be attracted to the detector and will offset the true ion current. The secondary electrons may be surpressed through the addition of repelling grids, but this also adds another source for secondaries. Robust RPA designs often have several grids at various potentials in an attempt to minimize these effects. Secondary electrons emitted from the detector plate itself may also escape and be interpretted as additional ion current. A *Faraday cup* configuration for the detector plate helps to mitigate this problem by providing a geometry from which electrons find it difficult to escape.

The second problem occurs because the retarding field is applied to a grid. The potential in the holes of the grid is not even. When the grid potential is higher than ambient potential, the field "sags" in these holes.[31,32] Thus, some ions with insufficient energy to pass through the potential set on the grid wires themselves will be able to pass through the lower potential presented in the holes of the grid. This has two effects on the trace. First, the EDF is artificially shifted toward higher energies. Second, an artificial broadening of EDF features occurs as the critera for an ion to reach the detector now depends not only on the retarding potential, but also slightly on the position in the grid through which the ion passed.

While there are several techniques available to correct this,[33,34] in our case we are using the RPA only to assure ourselves that the beam energy has the energy set by the acceleration voltage. Therefore it is merely necessary to understand that these effects are present and to account for them when analyzing the RPA data.

The maximum sag, ΔV, occurs in the center of the grid hole and is a function of the grid wire radius, r, the grid wire spacing, a, and the distance between the grid and the grounded detector plane, d. It is given by:

$$\frac{\Delta V}{V} = 1 - \frac{2\pi(d/a) - \ln 4}{2\pi(d/a) - 2\ln\left[2\sin(\pi r/a)\right]}. \tag{2.10}$$

In our experiments, the question is, “Given a beam with an expected energy of E, what is the maximum potential $V_{g_{max}}$ that will be read by our RPA?” Or, to put it another way, “At what potential $V_{g_{max}}$ will a beam particle with energy E be able to pass through the grid only where the field is lowest?” This potential is given by

$$E = qe\left(V_{g_{max}} - \Delta V_{g_{max}}\right). \tag{2.11}$$

Multiplying Equation 2.10 through by $V = V_{g_{max}}$, rearranging, and substituting into Equation 2.11 yields

$$E = E_{g_{max}} \frac{2\pi(d/a) - \ln 4}{2\pi(d/a) - 2\ln\left[2\sin(\pi r/a)\right]}, \tag{2.12}$$

where $E_{g_{max}} = qeV_{g_{max}}$, the energy corresponding to the grid voltage, has been used. This may be further manipulated to yield the maximum fractional increase in measured energy versus the actual beam energy,

$$\frac{\Delta E_{g_{max}}}{E} = \frac{E_{g_{max}} - E}{E} = \frac{2\pi(d/a) - 2\ln\left[2\sin(\pi r/a)\right]}{2\pi(d/a) - \ln 4} - 1. \tag{2.13}$$

Therefore, one would expect a monoenergetic beam of energy E to be spread between E and Eg_{max} when measured with an RPA.

The RPA in this experiment consists of a Faraday cup preceded by two grids. The Faraday cup was 12.7 mm in diameter. A 11.8 lines-per-cm sweep grid (78.7 lines-per-cm for the electron experiment) was positioned ~ 4 mm in front of the Faraday cup. The wire diameter was approximately 60 μm. A third grid was positioned another 4 mm in front of the sweep grid and was held below ground to reject secondary electrons emitted from the sweep grid. A Keithley 617 electrometer with a maximum resolution of 100 aA (typical resolution for the current levels of this experiment was 10 pA) measures the current incident in the cup. The grid closest to the cup is the sweep grid. The remaining grid is held at ground. The sweep grid controlled by an SRS PS350 analog programmable DC power supply capable of 5 kV. The power supply accepts a 0-10 V analog input to control its output voltage over its full range. The input is driven by a National Instruments DAQPad 6020E digital-to-analog converter. A LabVIEW program drives the power supply over the desired voltage range and reads the current measurements from the electrometer over a GPIB interface. Multiple measurements are taken at each voltage and averaged to improve accuracy.

The RPA traces were analyzed immediately to provide confirmation of beam energy. Figures 2.6 and 2.7 show the energy distribution functions (EDFs) of the beams, as measured by the RPA. They are plotted versus normalized energy, E/E_{nom}, where E_{nom} is the nominal beam energy as set by the ion source voltage. The energies that were passed by the RPA correspond with E and $E_{g_{max}}$, respectively. Substituting the dimensions of the RPA into Equation 2.13 we arrive at a value of

$$\frac{\Delta E_{g_{max}}}{E} = 11.1\%, \tag{2.14}$$

which actually overestimates the spread seen in the figures. This overestimation is likely due to the cup geometry of the RPA. Equation 2.13 is strictly valid only for a parallel plate detector. The electric field at the entrance to the cup is expected to "bulge" toward the grid, thus decreasing the sag of the grid. In any case, the spread of the beam can be primarily attributed to RPA effects, giving confidence that the ion beams were at the specified energies.

Many of the EDFs, particularly those at higher energies, show some non-monotonic behavior on either side of the peak. These local minima are the result of experimental

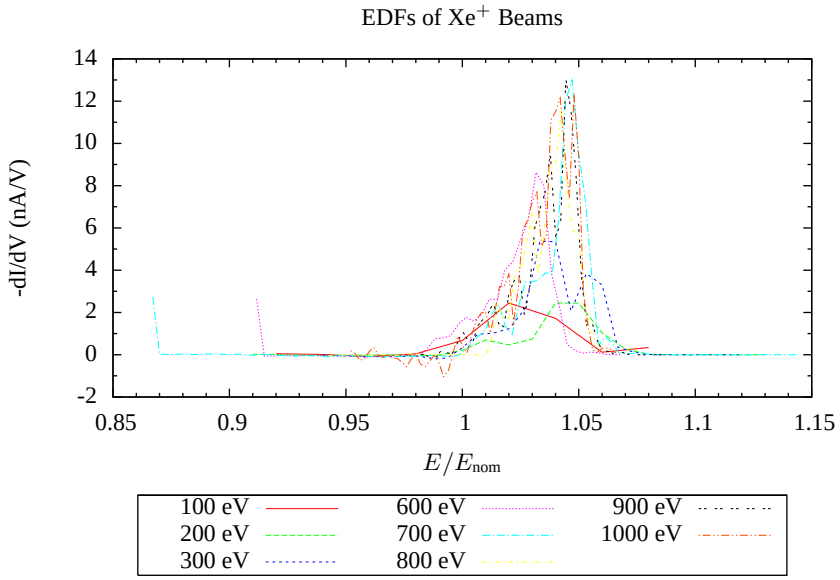

Figure 2.6: Energy distribution functions of the Xe^+ beams

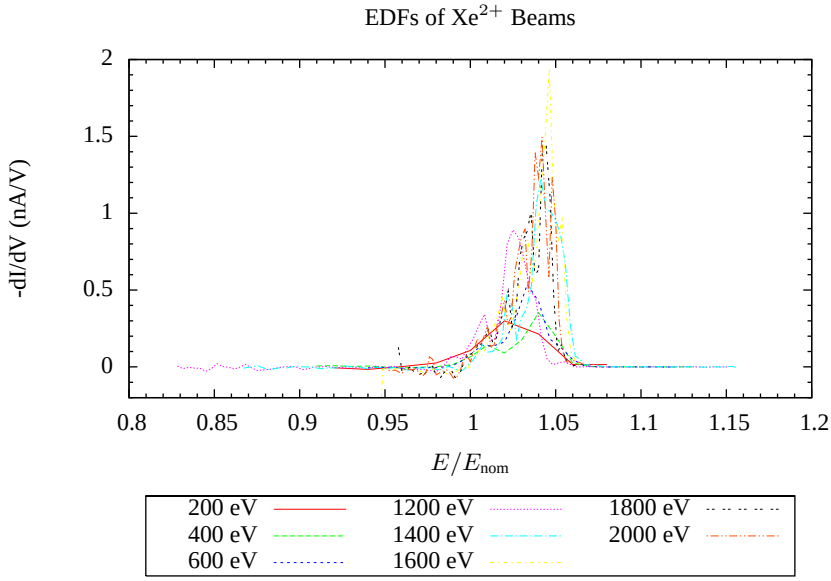

Figure 2.7: Energy distribution functions of the Xe^{2+} beams

oversampling. The power supply used to obtain these data was capable of only two volt resolution. However, the original data were sampled at a much higher resolution, resulting in a stepsize RPA trace. When the numerical derivative is applied (Equation 2.8) the resulting EDF has a "cut mountain" look. To correct for this error, the original RPA data have been resampled at two volt steps. This process is not entirely perfect, and some evidence of the original error remains. However, for the purpose of these data the results are sufficiently accurate.

2.3 Software

A large amount of data was acquired in the process of these experiments. Approximately 100 individual spectra were required, all of which needed to be acquired, stored, and then processed. Futhermore, these experiments represent the beginning of futher studies which will require similar processing. Therefore, both the acquisition itself as well as the processing involved substantial software development. This section is devoted to the explanation of some of the more interesting aspects of the software.

The software for these experiments was developed almost entirely using National Instruments LabVIEW. LabVIEW's main advantages are easy integration with scientific hardware and rapid development. One disadvantage of LabVIEW is that its code, which is graphical, does not lend itself well to print publishing. Therefore, the code is not included in this thesis. Readers interested in the code should contact the author.

2.3.1 Data acquisition

The main piece of software necessary for data acquisition was a program to control the CCD detector, acquire the images, and save them to disk. This program, while quite large, is rather uninteresting. It provides a user interface that allows the experimenter to configure the various acquisition settings such as exposure time, detector sensitivity, and so forth. The experimenter then triggers the acquisition, the results of which are displayed. The resulting data along with all parameters necessary for interpreting it are then saved in a binary format on disk.

2.3.2 Data processing

The data processing algorithms developed for these experiments contain the interesting scientific work. There are several commercial software packages available that perform similar processing of spectral data. However these packages are relatively expensive for a single user. For instance, Thermo Electron provides a suite of packages which runs approximately $2000 at the academic discount price in 2006.* Furthermore, canned algorithms do not easily allow for extension and correction, should that be necessary. The algorithms developed for this work will be further discussed in the Chapter 3.

*Prices from Thermo Electron Corporation company website, www.thermo.com, accessed March 20, 2006

2.3.3 Data storage

One challenge that became apparent early in the development of the processing algorithms was that the binary format originally developed for the acquisition software was difficult to manage. The HDF5 scientific data library* was therefore incorporated into the software and the original binary format converted to the HDF5 format.

In order to do this a LabVIEW interface to the HDF5 library was developed. The details of this interface are beyond the scope of this thesis. However, the resulting data structure enabled significantly easier batch processing of the experimental data.

2.4 Procedure

2.4.1 Ion collision experiment

Each experiment consisted of the following steps taken once the chamber was at vacuum:

1. Pressurize the ion source chamber with neutral xenon
2. Initiate a discharge in the ion beam source
3. Tune the discharge so that the voltage is sufficient to allow free electrons to gain enough energy to produce the desired ions (either first or second ionization stages of xenon, 12.1 eV and 21.0 eV respectively).[35]
4. Tune the acceleration voltage of the ion beam to the desired beam energy
5. Maximize the ion current reaching the Faraday cup by tuning the Wien filter and ion optics
6. Measure the ion current on the Faraday cup and cell wall
7. Take an RPA trace to measure the ion beam energy distribution function and verify the beam energy
8. Pressurize the collision cell with neutral xenon
9. Measure the ion current on the Faraday cup and cell wall
10. Determine appropriate exposure times to ensure sufficient signal-to-noise ratios
11. Acquire the emission spectra across the range from 700 nm to 1000 nm

2.4.2 Electron collision experiment

For the electron collision experiment we followed exactly the same procedure as the ion collision experiment, with the exception of creating the beam. Creating the electron beam is much simpler and involves the following steps

1. Heat the emitter filament by running current through it

*http://hdf.ncsa.uiuc.edu/

2. Bias the filament at the desired beam energy below the target
3. Tune the electrostatic lenses to maximize beam current and minimize divergence

From here we proceded exactly as in the ion experiments starting at Step 6.

Chapter 3

Analysis

The raw data produced by the experiment are the collision-induced emission spectra, the background intensity spectra, and the halogen-tungsten spectra. In order to cover the spectral range from 700 nm to 1000 nm, at each energy and target gas pressure the data were taken at three spectrograph grating angles. The angles are identified by the spectrograph micrometer setting, n, which was set to either: $n = 735$, $n = 825$, or $n = 915$. These numbers roughly correspond to the central wavelength of the spectrum acquired.

The raw data must be constructed into physically meaningful spectra and then the spectral peaks resulting from the emissions of interest must be measured. Specifically the following steps must be taken:

1. Remove cosmic ray spikes
2. Remove the background signal
3. Map the detector pixel to the spectral wavelength
4. Correct the spectra for the sensitivity of the spectral system
5. Identify the peaks of interest
6. Measure the area of the peaks of interest

Figure 3 shows sample raw emission data and illustrates the corrections that need to be addressed.

Once the area of the peaks is determined, the cross sections are calculated. This involves three steps:

1. Calculate the relative cross section from the peak area
2. Determine a scaling factor to relate relative cross section data to absolute cross section data
3. Apply the scaling factor to the relative data

The remainder of this chapter discusses each of the enumerate steps in detail.

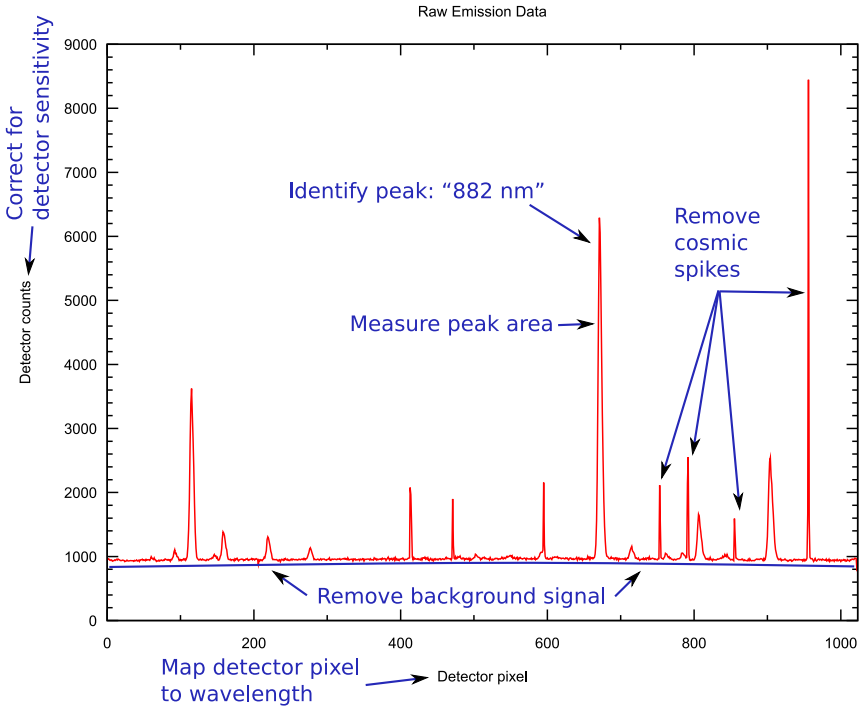

Figure 3.1: Sample raw emission data. The corrections and calculations needed are illustrated.

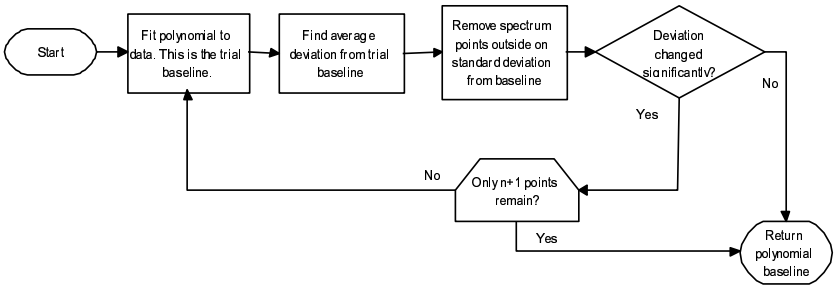

Figure 3.2: The baseline detection algorithm

3.1 Processing of raw spectra

3.1.1 Common algorithms

Two algorithms are reused at multiple points in the overall procedure. These are discussed first, before moving on to the previously enumerated algorithms.

Baseline removal

Most of the steps in the analysis require charactarization of the peaks present in the spectra. Therefore, accurate detection of these peaks is required. In order to accurately detect and measure peaks, the baseline from which the peaks stand needs to be identified and subtracted. In the final data this is done by subtracting a measured baseline signal that is acquired from the experimental setup while no collisions are occurring. However, in processing the data it is necessary to detect and remove the baseline without the benefit of an experimental background dataset. One place where this is obviously necessary is when removing peaks caused by cosmic rays in the background data itself.

As shown in Figure 3.2, the algorithm is iterative. It begins by fitting a polynomial of user-specified order, n, to the *entire* spectrum. In these experiments a quadratic function was found to be sufficient. The resulting polynomial is the first trial baseline. The procedure next calculates the average deviation of every point from the trial baseline. Any points which fall above one standard deviation from this average are discarded. A new trial baseline is then calculated by repeating the fit on the remaining data. This process repeats until the standard deviation of the points from the trial baseline changes less than a user-specified amount, typically 1%, from one iteration to the next. If this condition is not met, the algorithm will also exit if $n + 1$ or fewer points remain in the dataset.

The resulting polynomial is then subtracted from the spectrum, yielding a $y = 0$ baseline. Measurements of peak heights occuring in different portions of the spectrum may then be accurately compared.

The algorithm works very well for the relatively sparsely populated spectra encountered in these experiments. However, if the algorithm were to be used on more

heavily peaked spectra, the process of throwing away data outside one standard deviation might cause points that were actually along the baseline to be removed. This problem could be overcome by removing only data that deviate positively from the trial baseline, presuming that no significant "negative peaks" were present.

Peak detection

There are two types of peaks present in the raw spectra: true emission peaks resulting from electronic transitions and cosmic ray spikes. Regardless of the type of peak, all are detected with LabVIEW's peak detection algorithm. This algorithm characterizes peaks by fitting them to a quadratic function. The peak location in the x (pixel) and y (detector count) axes are determined by this algorithm, along with the second derivative, y''. Using these data, one can determine where the fit parabola intersects the baseline which yields an approximate width of the peak, w, according to

$$w = 2\sqrt{2\frac{y}{y''}}. \tag{3.1}$$

3.1.2 Cosmic spike removal

Cosmic radiation that passes through the atmosphere may be detected by the CCD. These rays typically generate large signals when they impact the detector. Naturally, longer exposures are typically subject to more such events. These anomolous spikes interfere with the accurate calculation of emission peak area if they overlap the true emission peak. Therefore, they must be removed.

Cosmic ray spikes are easily identifiable to the human observer. The rays typically affect between one and five pixels (in full vertical binning mode) and are thus very narrow. This sets them appart from the typically broader spectral peaks.

There are several strategies for handling cosmic spikes. Most strategies involve comparing multiple spectra of the same source and removing anomolous peaks that only show up in one spectrum. Multiple spectra may be acquired through multiple exposures. Alternatively, they can be acquired taking multi-track measurements with a CCD detector. With this method, each horizontal track generates is own spectrum. Using a multiple spectra algorithm requires additional total exposure time. For multiple exposures, additional time is required for each exposure. For multi-track measurements, the sensitivity of each track is a fraction of the total sensitivity. Therefore, in order to achieve signal levels comparable to a signal track, the exposure time must be increased.

The software provided with the Andor iDus detector has a multi-exposure comparison algorithm built into it, and this algorithm has been used. However, for reasons which are unclear, the algorithm did not remove all cosmic spikes from the spectra. Therefore an additional algorithm was developed.

The post-acquisition algorithm does not have the benefit of comparing multiple spectra. Therefore, it relies on identifying the cosmic spikes the same way a human observer does—by how narrow it is. The first step in the algorithm is to find and remove the baseline using the algorithm discussed in Section 3.1.1. This is of critical

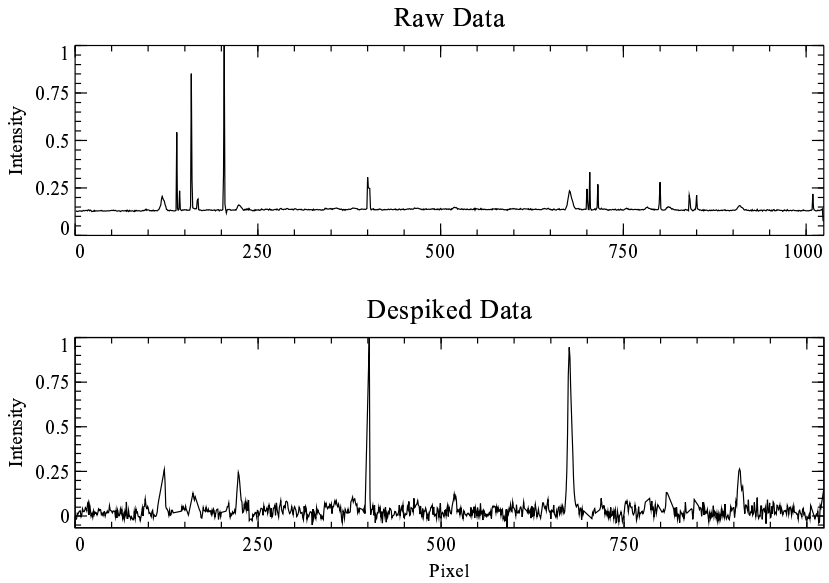

Figure 3.3: Sample input and output for the cosmic ray spike removal algorithm

importance because the algorithm will find peaks above a certain threshold level. In order for that to function correctly, all of the peaks need to start from the same level.

Using the LabVIEW peak detection algorithm, the approximate width of all peaks in the spectra are calculated according to Equation 3.1. The calculated width of the pixels is compared against the cosmic ray width critera, which typically is $w \leq 3$. The data associated with this peak is removed from the spectrum.

Sample results of the algorithm are shown in Figure 3.3. The reader will note that one cosmic spike remains in this particular case. It is acceptable for a few spikes to remain, so long as they do not interfere with any of the spectral peaks of interest. Because of the possibility of the algorithm missing some cosmic spikes, the final resulting data must be checked for sensibility. Cross sections that seem unduly large may be a result of a missed cosmic spike which overlapped an emission peak.

In some cases it is necessary to interpolate data in the excised portion of the spectrum. For instance, when subtracting experimental background data from the emission data, the background data must be complete. In these cases, the missing data is recreated by linear interpolation between the points remaining at either edge of the excised peak.

3.1.3 Subtraction of the background signal

Once cosmic spikes have been removed from both the emission and the background data, the background data, $B_n(x)$, is subtracted pixel-by-pixel from the raw emission

Micrometer	a	b	$c \times 10^6$	$d \times 10^9$
735	717.484	0.118507	-8.44154	-0.817887
825	810.187	0.112872	-8.28832	-1.32005
915	902.677	0.108883	-14.7028	2.77278

Table 3.1: Cubic fit parameters for pixel-to-wavelength calibration

data, $R_n(x)$:

$$R_n(x) - B_n(x) \tag{3.2}$$

3.1.4 Pixel-to-wavelength calibration

The detector returns the spectra as detector counts versus pixel position. These need to be mapped to the real units of photons-per-second versus wavelength. To map the raw spectra from pixel to wavelength, the peak detection algorithm identifies the center of prominent emission peaks. The peaks are presented graphically to the user, who then manually labels then according to the corresponding transition wavelength, creating a wavelength versus pixel table. A cubic fit is then applied to the table. The mapping function, $\lambda(x)$, is the resulting polynomial function,

$$\lambda(x) = a + bx + cx^2 + dx^3 \tag{3.3}$$

where $a, b, c,$ and d are the parameters of the fit. This functional form is used to map all raw spectra from functions of pixel, to functions of wavelength.

Figure 3.4 shows the known datapoints along with the best fit cubic curve for each of the micrometer settings used in the experiments. Table 3.1 shows the fit parameters for each of the settings.

One can see that there is excellent agreement between the datapoints and the fit. There is high confidence in the accuracy of this portion of the calibration. However, it should be noted that the accuracy of these calibrations does not affect the measurement of the cross sections so long as they are adequate to allow for the proper identification of spectral lines. This means that they can be no more than about 2.5 nm off at any point, as the closest lines in this study are 5 nm apart (the 823 nm and 828 nm lines). The proper detection of the peaks shows that these calibrations are sufficiently accurate.

3.1.5 Spectral sensitivity calibration

The CCD detector returns intensity data as detector counts. Detector counts are directly proportional to the number of photons detected by the CCD. However, due to non-uniform pixel sensitivities, the wavelength dependence of the CCD sensitivity, and the wavelength dependence of the spectrograph grating reflectivity and optical transimission elements, the spectrograph needs to be calibrated at each grating position (micrometer setting) in order to correct the raw spectra.

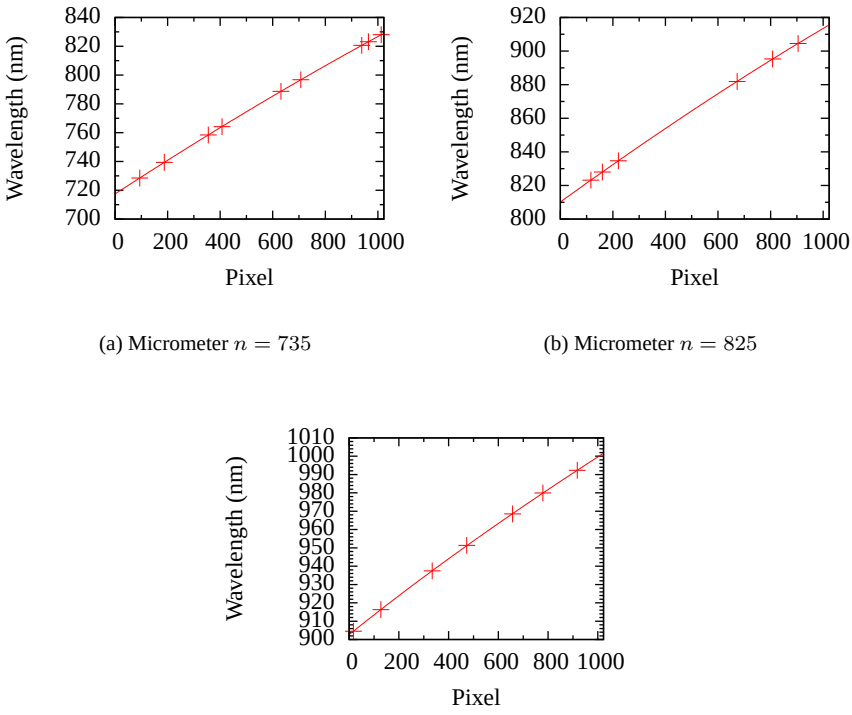

(a) Micrometer $n = 735$

(b) Micrometer $n = 825$

(c) Micrometer $n = 915$

Figure 3.4: The pixel-to-wavelength calibration data and cubic fits

The emissions from a halogen-tungsten lamp are used to calibrate the spectral response of the system. The actual spectrum of the lamp is assumed to be the Planck distribution for the temperature of the filament. The acquired lamp spectrum, $W(x)$, is expressed as a rate by dividing by the exposure time, t. The detector amplification, s_d, a scalar setting of the detector, must also be considered. The Planck distribution, $W_T(\lambda)$ for the filament temprature is divided by the resulting quantity, yielding the overall sensitivity of the system as a function of detector pixel (or wavelength):

$$s_n(x) = \frac{tW_T\left(\lambda(x)\right)}{s_d W(x)}, \tag{3.4}$$

where $W_T(\lambda)$ is the Planck distribution in photons/(m^3 s)[36]

$$W_T(\lambda) = \frac{2c}{\lambda^4\left[\exp\left(\frac{hc}{\lambda kT}\right) - 1\right]}. \tag{3.5}$$

Given the raw spectrum at micrometer setting n, $R_n(x)$ and the background spectrum, $B_n(x)$ and using Equation 3.4 the corrected spectrum, $I_n(x)$, is thus defined as

$$I_n(x) = s_n(x)\frac{s_d\left[R_n(x) - B_n(x)\right]}{t}. \tag{3.6}$$

Figure 3.5 shows the results of the halogen-tungsten lamp measurement plotted with the Planck distribution for the lamp at 3065 K. The data acquired on different micrometer settings are plotted in different colors. Figure 3.6 shows the resulting sensitivity curve that is multiplied by the raw collision emission data to calculate the cross-sections.

One interesting aspect of the sensitivity curves is that the last two pixels of the detector are very insensitive. There are two possible explanations for this:

1. The image in this region was occluded by some portion of the spectrograph internals, such as the focusing tube
2. There is a manufacturing flaw in these pixels of the detector

However, I did not pursue the investigation further. Rather, peaks occuring in the high pixels of the detector are not counted as reliable. In practice, this is not a large limitation as any peak crossing these last two pixels is most likely incomplete, and therefore not quantitatively useful.

3.1.6 Peak identification

Having corrected each of the spectra, the peaks corresponding to the transitions of interest must be identified and their total areas measured. Once again, LabVIEW's peak detection algorithm is employed. In this operation, it returns only those peaks which are higher than a user-specified threshold. This threshold was typically one-half of a standard-deviation in these experiments.

The list of detected peaks is then compared against a list of transitions of interest. For each known transition, the algorithm determines which detected peak is closest in

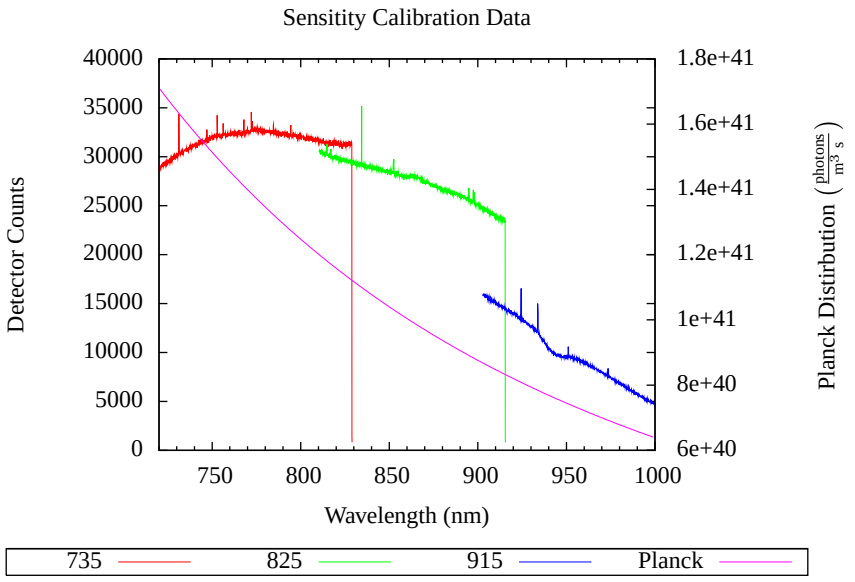

Figure 3.5: Raw sensitivity data and the Planck distribution for a 3065 K body.

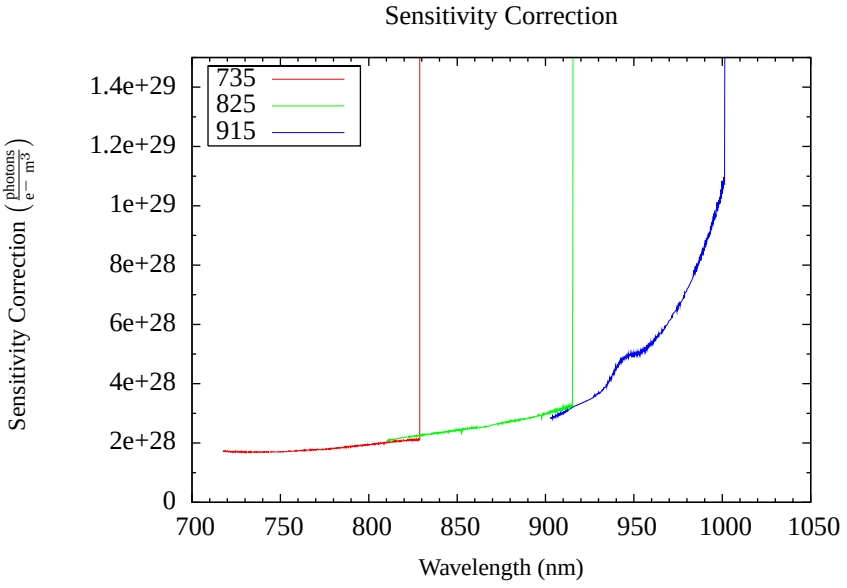

Figure 3.6: Sensitivity correction factor

wavelength. It then checks to see if the distance between the transition wavelength and the wavelength peak that was detected is within a user-specified amount. Typically this distance was 3 nm.

This algorithm is not particularly robust. However, because the data acquired in these experiments is relatively noise-free, and because there are a limited number of peaks, it works sufficiently well. Future experiments, particularly those that view less-pure species or those in more crowded regions of the spectrum, may require a more sophisticated algorithm.

3.1.7 Numerical peak measurement

The first step in measuring the peak is to determine its width. The algorithm begins by using the approximate width determined from the peak detection second derivative (see Equation 3.1). It starts half this width from the peak center. It then steps outward, first in one direction and then the other, until it reaches a datapoints with values greater than the previous point. The previous point is then determined to be the extent of the peak.

The obvious flaw in this algorithm is that any spurious noise could potentially cause the width the edge finding loop to abort prematurely. In application, however, the edge finder only provides small corrections to the width already estimated by the second derivative. These corrections are even more minimal considering that the bulk of the peak area is in the middle of the peak, and not at the edges.

Once the edges of a peak are determined, the peak area is calculated via trapazoidal numerical integration. For the peak at wavelength λ extending from pixel x_0 to pixel x_f, the area of the peak, P_λ, is

$$P_\lambda = \sum_{x=x_0}^{x_f} I_n(x). \tag{3.7}$$

3.1.8 Double-gaussian peak measurement

In addition to simple numeric integration, I also investigated fitting the data to a known functional form in an effort to squeeze out more accurate information from relatively few points of data. Several forms were tried, but a double Gaussian was eventually chosen.

The original line shape of the spectral peaks was assumed to be that of the Voight profile, a convolution of the Lorentzian profile created by the natural line width of the transition, and the Gaussian profile caused by collisional and Doppler (temperature) effects.[37] In addition, there are Gaussian measurement errors caused by the measurement system itself—mostly a result from the finite slit width in the detector.

In these experiments the Gaussian profile from the Doppler broadening was expected to swamp the Lorentitzian contributions. Even were it not the case, the measurement error contribution to the profile also overpowers the Lorentzian. Thus, we expected that the peak profile would be well described by a Gaussian.

However, the peaks presented did not fit a Gaussian profile well. Investigation into the qualities of the spectrograph revealed that the device had a certain amount of "double-vision." Figure 3.7 shows an image of the slit taken by the detector with the grating turned to zero-order, where it acts simply as a mirror. The light source was ambient room light. The detector was rotated by 90 degrees from its normal operating position in order to image the entire slit. One would expect to see a single, clear line, perhaps slightly curved due to the optics of the spectrograph. However, the image clearly shows two lines. The source of the second image was never found, though distortion in the spectorgraph optics was determined to be the only possible cause, after ruling out the grating and the slit. After the experiments covered by this thesis were complete, a realignment of the optics eliminated the problem. However, at the time of the experiments we were not equipped to perform this delicate task. Because of the double image, the peaks in these spectra were actually made up of the addition of two Gaussians, rather than a single one. Therefore, I developed software to fit the peaks to the form:

$$y(x) = \frac{a_1}{\sigma\sqrt{2\pi}} \exp\left[\frac{-(\lambda-\lambda_0)^2}{2\sigma^2}\right] + \frac{a_2}{\sigma\sqrt{2\pi}} \exp\left[\frac{-(\lambda-\lambda_0-\Delta\lambda)^2}{2\sigma^2}\right] \quad (3.8)$$

where a_1, a_2, σ, λ_0 and $\Delta\lambda$ are adjustable parameters. The fits were performed using the Levenburg-Marquardt algorithm. Because the Gaussian is normalized, once the fit is performed, the area is calculated by

$$P_\lambda = a_1 + a_2. \quad (3.9)$$

Figure 3.7: Distorted slit image

The algorithm worked very well most of the time. However, if any negative points were contained in the fit, as could happen once the background data were subtracted from the emission signal, the fit procedure returned wildly erratic results. This shortcoming could be relatively easily corrected, for instance, by throwing away negative values. However, because the trapazoidal integration appeared sufficient, the double-Gaussian fit method was eventually abandoned, and all of the results in this thesis have been calculated with strict numerical integration.

3.2 Cross section calculation

Recall the basic expresion for a cross section

$$\sigma = \frac{I}{LQ_b n}. \tag{1.31}$$

To calculate the cross section we need to first relate these quantities to the directly measureable quantities. The corrected measured peak intensity is related to the total peak intensity by the view factor, f, according to

$$P_\lambda = f I_\lambda. \tag{3.10}$$

The total beam current is the sum of the current collect by the Faraday cup and the current collected on the back wall of the collision cell:

$$I_b = I_f + I_w, \tag{3.11}$$

may be expressed in particles per second as

$$Q_b = \frac{I_b}{qe}. \tag{3.12}$$

The pressure and number density are related by an equation of state. The specific form will ultimately not be relavent so long as the temperature of the target gas remains constant, but we will use the ideal gas equation an example:

$$P = nRT \tag{3.13}$$

Subsitituting Equations 3.10 to 3.13 into Equation 1.31, the cross section is given by

$$\sigma_\lambda = \frac{qeP_\lambda}{(fL/RT)\,PI_b} \tag{3.14}$$

The term in parentheses contains several factors which are not measured in these experiments, but which should remain constant from transition to transition and from one experiment to the next. The integrated peak height also contains an unknown geometry: the effective volume from which the blackbody radiation used to calibrate the sensitivity was emitted. For the sake of correct units, this factor must also be added into G. These factors are all collected, yielding:

$$G \equiv \frac{fL}{RTV_{\mathrm{BB}}} \tag{3.15}$$

and Equation 3.14 is simplified to:

$$\sigma_\lambda = \frac{qeP_\lambda}{GI_bP}. \tag{3.16}$$

3.3 Geometric correction factor

Equation 3.16 contains the unknown factor G which much be determined experimentally. In order to calculate G, experiments have been conducted that duplicate previously published data. The results are calculated as far as possible, given that G is still unknown, yielding the "relative cross section", ξ_λ which is given by:

$$\xi_\lambda \equiv G\sigma_\lambda. \tag{3.17}$$

These relative cross sections are then compared against published cross sections and G is determined.

$$G = \frac{\xi_\lambda}{\sigma_\lambda} \tag{3.18}$$

G may be thought of as a characteristic length of the experimetal setup because contains only constants which are specific to the geometry of the experiment, and a temperature which is expected to change negligibly. Therefore, a G value determined from one data set should be applicable to all other data sets produced from the same experimental setup.

Two data sets are available for comparison. The first are electron impact excitation cross sections for 30 eV electron beams. The absolute cross sections were determined experimentally and published by Fons and Lin.[27] The second dataset is the 300 eV ion impact emission cross sections, which were published by Chiu.[24]

3.3.1 Electron impact cross section comparison: theory

The electron impact data are reduced according to Equation 3.16, except that the unknown G is not included. These data, as well as Fons and Lin's cross sections, σ_λ, are fitted to a function of pressure so that zero-pressure cross sections may be extrapolated.[24]

$$\xi_\lambda(P) = \xi_\lambda(0)\left[1 + a\left(\frac{E - 11.5\text{ eV}}{E - 9.8\text{ eV}}\right)^n \left(1 - e^{-\gamma P}\right)^2\right], \tag{3.19}$$

and likewise,

$$\sigma_\lambda(P) = \sigma_\lambda(0)\left[1 + a\left(\frac{E - 11.5\text{ eV}}{E - 9.8\text{ eV}}\right)^n \left(1 - e^{-\gamma P}\right)^2\right]. \tag{3.20}$$

It is important to compare zero-pressure cross sections because the effects of radiation trapping (see Section 1.3) are dependent not only on pressure but also on the optical path length through which the experiment is viewed. Since these path lengths are not consistent between my experiment and that of Fons and Lin, equal pressures do not correspond to equal radiation trapping.

The zero-pressure cross sections determined by the fit are then compared and G value calculated for that line. Because Fons and Lin's data are excitation cross sections into the upper states, my emission cross sections must be divided by the branching ratio

Upper level	Wavelength (nm)	Micrometer	$\xi_\lambda(0)$ $\left(\times 10^{-20}\text{cm}^2\right)$	a	n	γ
2p6	823.16	825	13.6757	0.781831	3.60327	2.00401
2p6	823.16	735	17.4987	0.569381	5.91320	1.53880
2p5	828.01	825	25.6127	1.00406	0.699347	1.70387
2p5	828.01	735	24.6310	1.10481	-0.0404637	1.47001
2p3	834.68	825	6.56555	0.664505	3.64586	2.11734
2p7	840.92	825	13.8567	0.784236	24.0240	-0.00615232
2p8	881.94	825	13.6167	0.700157	4.49749	1.73223
2p6	895.23	825	11.4933	0.953025	-1.02110	2.11720
2p9	904.54	825	19.0978	1.01725	1.08654	1.96638
2p9	904.54	915	20.9929	0.733852	3.64093	1.19881
2p7	916.27	825	2.33522	-43.2048	-69.2678	-0.00439138
2p7	916.27	915	9.05979	1.49819	-2.94639	1.43524
2p10	979.97	915	6.38626	0.704122	2.42774	1.05306
2p9	992.32	915	17.5496	0.740598	3.62489	1.52313

Table 3.2: Parameters of the best fit to 30 eV e− + Xe data

in order to make a meaningful comparison:

$$G_\lambda = \frac{\xi_\lambda(0)}{f_\lambda \sigma_\lambda(0)}. \tag{3.21}$$

The "λ" subscript has been added to G because this is the G value calculated from one line. Because G depends only on experimental geometry, it should be independent of wavelength. Therefore

$$G = \overline{G_\lambda}. \tag{3.22}$$

3.3.2 Electron impact cross section comparison: results

The electron impact emission cross section experiment was designed to enable the scaling of the relative cross sections acquired by our experiments to absolute cross sections published by Fons and Lin. However, as this section shows, the results of this analysis conflicted with other data, and was therefore ultimately discarded in favor of a simpler method of scaling.

As discussed in Section 3.3, only at zero-pressure can one experiment be compared to another in a valid fashion. Figures 3.8 and 3.9 show the relative cross sections derived from my data, and the absolute cross sections from Fons and Lin, respectively. Each data set is plotted as a function of pressure for each transition. The fit lines correspond to the best fit function of the form of Equation 3.19. The parameters for these fits are shown in Tables 3.3 and 3.2. Of particular interest is the zero-pressure cross-section, $\sigma_\lambda(0)$. The G factor is calculated utilizing Equations 3.21 and 3.22, and the results are listed Table 3.4.

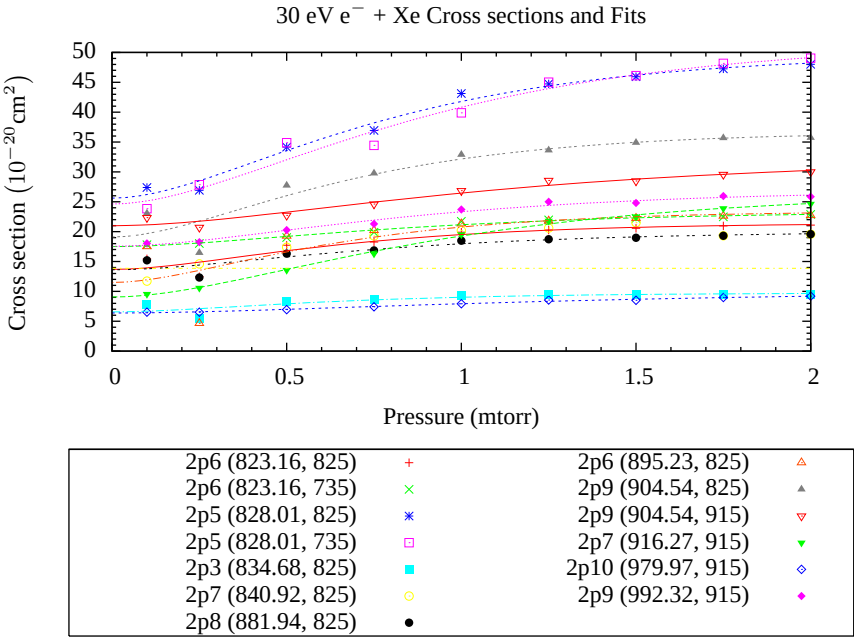

Figure 3.8: 30 eV relative cross sections and their best fits

Upper level	$\sigma_\lambda(0)$ $(\times 10^{-20}\text{cm}^2)$	a	n	γ
2p1	424.345	0.369705	9.85076	1.33074
2p3	333.424	7.01070	-21.8760	0.0252797
2p5	1640.29	0.506226	5.69471	1.77973
2p6	696.341	0.554701	6.39726	0.743697
2p7	618.613	1.11497	-0.272933	1.65553
2p8	559.531	0.402034	10.2736	1.27119
2p9	1084.32	0.885176	2.16071	1.40828
2p10	367.694	0.851605	2.61463	1.58465

Table 3.3: Parameters of the best fit to the Fons and Lin data

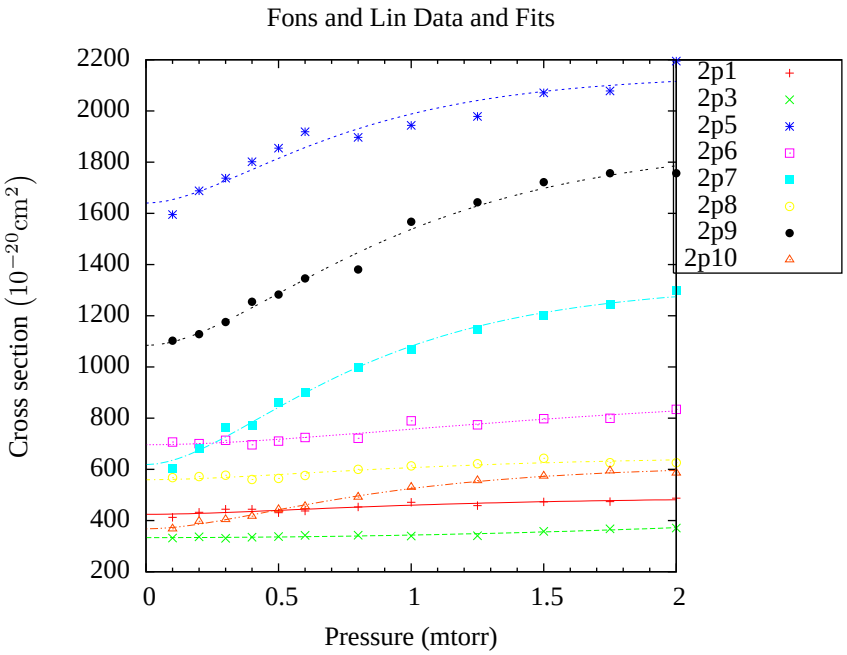

Figure 3.9: Fons and Lin cross sections and their best fits

Upper level	Wavelength (nm)	Micrometer	$\xi_\lambda(0)$ (cm^2)	$\sigma_\lambda(0)$ $(\times 10^{-20}\text{cm}^2)$	$G \times 10^{-18}$
2p6	823.16	825	16.2616	696.341	2.33529
2p5	828.01	825	25.6341	1640.29	1.56278
2p3	834.68	825	6.56552	333.424	1.96912
2p8	881.94	825	13.6090	559.531	2.43222
2p6	895.23	825	11.6427	696.341	1.67198
2p9	904.54	825	18.7397	1084.32	1.72824
2p9	904.54	915	20.8906	1084.32	1.92661
2p7	916.27	915	12.8672	618.613	2.08002
2p10	979.97	915	6.85646	367.694	1.86472
2p9	992.32	915	19.8064	1084.32	1.82662
				Average	1.94
				Standard Deviation	0.264
				% Standard Deviation	%13.6

Table 3.4: G Factor calculation from e^- + Xe collision experiment comparison to Fons and Lin's data

Unfortunately, applying this G factor to the 300 eV Xe data and comparing them to the earlier results from Chiu reveals a difference of a factor of two. After thouroughly investigating the algorithms used in the G factor calculation and manually spot checking a few points, I concluded that the original data for the electron experiments was inaccurate.

The most likely source of this error is the current measurement. While operating the electron source, we had an extremely difficult time maintaining a small beam divergence. It is likely that the beam was so divergent that it lead to erroneous current measurements if portions of the beam did not hit either of the two detectors.

3.3.3 300 eV experiment comparison

Because of the failure of the e^- + Xe experiment I was forced to rely on the second method for scaling the relative cross sections. This method is much easier, but also less accurate, as it compares my 300 eV collision data to that of Chiu, who in turn compared her data to Fons and Lin. Furthermore, by using the 300 eV data for scaling, it eliminates the one set of data that might be used for validation against exisiting data.

Chiu found there to be very little pressure dependency for the ion collision cross sections. Therefore, simple comparison of the relative cross-sections to the published absolute cross sections, σ_λ yield the correct G_λ factors. Also, Chiu published emission cross sections rather than excitation cross sections, so there is no need to deal with branching ratios as in Equation 3.21. Therefore,

$$G_\lambda = \frac{\xi_\lambda}{\sigma_\lambda}. \tag{3.23}$$

Once again, Equation 3.22 is used to determine an overall G factor.

Table 3.5 shows the unscaled cross-sections from my 300 eV data, the data from Chiu, and the resulting G factors. The factors for the individual lines show decent agreement, consistent with the level that is expected in such experiments. The average G factor shown has been used in the calculation of the final cross sections.

3.4 Absolute cross sections

Once the G factor has been determined, the absolute cross sections are calculated throught the simple application of Equation 3.16. The results are presented in the next chapter.

Upper level	Wavelength (nm)	Micrometer	ξ_λ $\left(\times 10^{19}\mathrm{Pa}^{-1}\mathrm{m}^{-3}\right)$	σ_λ $\left(\times 10^{-24}\mathrm{m}^{2}\right)$	G $\left(\times 10^{40}\mathrm{Pa}^{-1}\mathrm{m}^{-5}\right)$
2p6	735	823.16	10.00	29.23	3.423
2p5	735	828.01	1.306	3.90	3.349
2p6	825	823.16	10.02	29.23	3.428
2p5	825	828.01	1.320	3.90	3.385
2p3	825	834.68	1.022	3.13	3.265
2p8	825	881.94	22.09	69.11	3.197
2p9	825	904.54	7.817	18.67	4.187
2p9	915	904.54	6.277	18.67	3.362
2p10	915	979.97	10.52	32.17	3.217
				Average	3.424
				Standard Deviation	0.2814
				% Standard Deviation	8.218%

Table 3.5: G values calculated from 300 eV Xe^+ + Xe data compared to the data publsihed by Chiu

Chapter 4

Results

4.1 Xe^+ + Xe

The determined cross sections for collisions between singly-ionized xenon and neutral xenon are listed in Tables 4.1 through 4.10. The excitation cross sections presented in the tables are calculated by dividing the reported emission cross section by the branching ratio. The data are also plotted versus energy in Figure 4.1. The cross sections show good agreement with Chiu's data for the 300 eV beam energy, as would be expected. Note that the data are not identical, despite the fact that these unscaled cross sections were used in determining the G factor, because an overall average G factor is used, rather than line-by-line G factors.

4.2 Error Analysis

The symbol σ is commonly used to denote standard deviations in error analyses. However, in order to avoid confusion with the symbol for cross sections, this analysis adopts the symbol $V(x)$ for the variance of quantity x and $\epsilon_{\text{std}}(x)$ for the standard deviation ($\sqrt{V(x)}$) of the same. Most errors will be expressed as fractional quantities in order to simplify combination which are denoted by the non-subscripted ϵ and given by:

$$\epsilon(x) = \frac{\epsilon_{\text{std}}(x)}{x} = \frac{\sqrt{V(x)}}{x} \tag{4.1}$$

The quantifiable sources of error in these experiments are, in decreasing order of importance:

1. The G Factor calibration
2. Beam current drift
3. Detector measurement error on the signal, background, and sensitivity curves

Following the order in which these errors propegate, the detector measurement error will be addressed first. The uniformity of the CCD detector used in these experi-

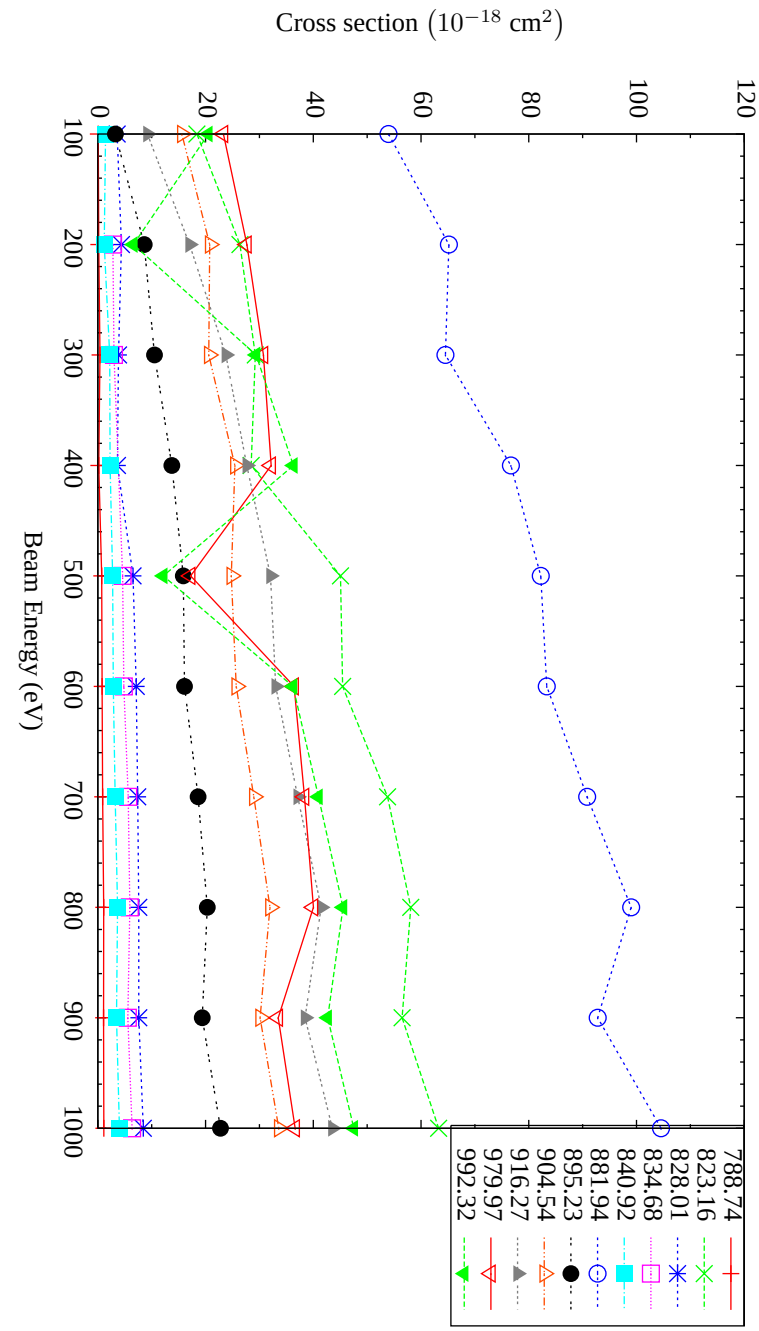

Figure 4.1: Cross sections for Xe^+ + Xe versus beam energy

Wavelength (nm)	Upper level	Branching ratio	Cross section ($\times 10^{-18}$cm^2)	Negative Deviation (%)	Positive Deviation (%)	Excitation cross section ($\times 10^{-18}$cm^2)	Notes
788.74	2p1	0.72	0.0813	9.6806	9.6809	0.1129	
823.16	2p6	0.74	18.3801	6.8153	10.4807	24.7376	1
828.01	2p5	1	3.6008	6.8152	20.5855	3.6008	1
834.68	2p5	1	-	-	-	-	3
840.92	2p7	0.1	1.4467	9.6346	53.9369	14.4665	
881.94	2p8	1	53.9481	9.6305	10.2081	53.9481	
895.23	2p6	0.24	3.2588	9.6382	73.5847	13.4109	
904.54	2p9	0.38	15.5997	6.8822	11.9687	41.1600	2
916.27	2p7	0.9	9.2081	9.6359	9.9992	10.2312	
979.97	2p10	0.98	23.3057	9.6301	9.9068	23.9033	
992.32	2p9	0.62	20.5160	9.6297	11.0107	33.0903	

Table 4.1: Cross sections for Xe^+ + Xe at 100 eV

Wavelength (nm)	Upper level	Branching ratio	Cross section ($\times 10^{-18}$cm^2)	Negative Deviation (%)	Positive Deviation (%)	Excitation cross section ($\times 10^{-18}$cm^2)	Notes
788.74	2p1	0.72	0.1848	9.6548	97.8376	0.2567	
823.16	2p6	0.74	26.3912	6.8172	9.7166	35.5197	1
828.01	2p5	1	4.3764	6.8572	15.0203	4.3764	1
834.68	2p3	0.86	2.7934	9.6349	19.7799	3.2368	
840.92	2p7	0.1	1.1897	9.6390	34.4722	11.8970	
881.94	2p8	1	65.1748	9.6311	9.6432	65.1748	
895.23	2p6	0.24	8.6227	9.6316	9.6492	35.4842	
904.54	2p9	0.38	20.7752	6.8986	9.5873	54.8158	2
916.27	2p7	0.9	17.0232	9.6306	9.8343	18.9147	
979.97	2p10	0.98	27.6851	9.6308	10.5853	28.3950	
992.32	2p9	0.62	6.5996	9.6411	13.3508	10.6446	

Table 4.2: Cross sections for Xe^+ + Xe at 200 eV

Wavelength (nm)	Upper level	Branching ratio	Cross section ($\times 10^{-18}$cm^2)	Negative Deviation (%)	Positive Deviation (%)	Excitation cross section ($\times 10^{-18}$cm^2)	Notes
788.74	2p1	0.72	0.3969	9.6362	65.0084	0.5512	
823.16	2p6	0.74	29.2442	6.8099	9.6982	39.3596	1
828.01	2p5	1	3.8359	6.8099	18.0147	3.8359	1
834.68	2p3	0.86	2.9851	9.6317	10.5693	3.4589	
840.92	2p7	0.1	2.2123	9.6553	10.0090	22.1231	
881.94	2p8	1	64.5258	9.6307	9.6743	64.5258	
895.23	2p6	0.24	10.5112	9.6302	10.2359	43.2560	
904.54	2p9	0.38	20.5834	6.8502	10.0462	54.3096	2
916.27	2p7	0.9	23.7535	9.6303	9.6321	26.3928	
979.97	2p10	0.98	30.7380	9.6299	9.9139	31.5262	
992.32	2p9	0.62	29.3721	9.6293	10.0345	47.3744	

Table 4.3: Cross sections for Xe^+ + Xe at 300 eV

Wavelength (nm)	Upper level	Branching ratio	Cross section ($\times 10^{-18}$cm^2)	Negative Deviation (%)	Positive Deviation (%)	Excitation cross section ($\times 10^{-18}$cm^2)	Notes
788.74	2p1	0.72	0.1700	9.6459	58.3662	0.2361	
823.16	2p6	0.74	28.4674	7.6604	8.5782	38.3141	1
828.01	2p5	1	3.6417	8.4429	14.9924	3.6417	1
834.68	2p3	0.86	-	-	-	-	3
840.92	2p7	0.1	2.2768	9.6318	10.8922	22.7675	
881.94	2p8	1	76.6946	9.6309	9.6312	76.6946	
895.23	2p6	0.24	13.7467	9.6306	9.6488	56.5708	
904.54	2p9	0.38	25.4529	6.8443	9.6363	67.1580	2
916.27	2p7	0.9	27.6542	9.6304	9.6312	30.7269	
979.97	2p10	0.98	32.1688	9.6301	9.6394	32.9936	
992.32	2p9	0.62	36.3195	9.6295	9.6446	58.5798	

Table 4.4: Cross sections for Xe^+ + Xe at 400 eV

Wavelength (nm)	Upper level	Branching ratio	Cross section ($\times 10^{-18}$cm^2)	Negative Deviation (%)	Positive Deviation (%)	Excitation cross section ($\times 10^{-18}$cm^2)	Notes
788.74	2p1	0.72	0.7124	9.6308	21.8524	0.9894	
823.16	2p6	0.74	45.0422	6.8137	9.6841	60.6221	1
828.01	2p5	1	6.5296	6.8681	14.7496	6.5296	1
834.68	2p3	0.86	4.6079	9.6316	10.0891	5.3393	
840.92	2p7	0.1	2.7573	9.6311	10.1650	27.5725	
881.94	2p8	1	82.2289	9.6306	9.6653	82.2289	
895.23	2p6	0.24	15.8708	9.6300	10.0344	65.3119	
904.54	2p9	0.38	24.7743	6.8186	10.0506	65.3675	2
916.27	2p7	0.9	32.0570	9.6304	9.8070	35.6189	
979.97	2p10	0.98	17.2319	9.6351	9.8352	17.6737	
992.32	2p9	0.62	12.1477	9.6376	9.8806	19.5931	

Table 4.5: Cross sections for Xe^+ + Xe at 500 eV

Wavelength (nm)	Upper level	Branching ratio	Cross section ($\times 10^{-18}$cm^2)	Negative Deviation (%)	Positive Deviation (%)	Excitation cross section ($\times 10^{-18}$cm^2)	Notes
788.74	2p1	0.72	0.7934	9.6287	14.0830	1.1020	
823.16	2p6	0.74	45.4559	6.8126	9.6765	61.1789	1
828.01	2p5	1	7.1264	6.8104	15.1485	7.1264	1
834.68	2p3	0.86	4.8153	9.6316	9.9677	5.5797	
840.92	2p7	0.1	2.8786	9.6315	10.4984	28.7861	
881.94	2p8	1	83.3384	9.6306	9.6565	83.3384	
895.23	2p6	0.24	16.0983	9.6300	11.1032	66.2481	
904.54	2p9	0.38	25.6915	6.8418	10.2077	67.7876	2
916.27	2p7	0.9	33.0176	9.6302	9.9129	36.6862	
979.97	2p10	0.98	36.4432	9.6298	9.7508	37.3776	
992.32	2p9	0.62	36.2373	9.6292	10.0094	58.4473	

Table 4.6: Cross sections for Xe^+ + Xe at 600 eV

Wavelength (nm)	Upper level	Branching ratio	Cross section ($\times 10^{-18}$cm^2)	Negative Deviation (%)	Positive Deviation (%)	Excitation cross section ($\times 10^{-18}$cm^2)	Notes
788.74	2p1	0.72	0.8928	9.6295	25.2024	1.2401	
823.16	2p6	0.74	53.7853	6.8175	9.7888	72.3893	1
828.01	2p5	1	7.3981	6.8124	16.7296	7.3981	1
834.68	2p3	0.86	5.6482	9.6316	10.2547	6.5449	
840.92	2p7	0.1	3.2290	9.6316	16.6075	32.2896	
881.94	2p8	1	90.8534	9.6306	9.6607	90.8534	
895.23	2p6	0.24	18.6056	9.6300	10.1970	76.5663	
904.54	2p9	0.38	28.9493	6.8480	10.0206	76.3834	2
916.27	2p7	0.9	37.0917	9.6302	9.8045	41.2130	
979.97	2p10	0.98	38.3545	9.6298	9.7484	39.3379	
992.32	2p9	0.62	40.9591	9.6292	9.8248	66.0631	

Table 4.7: Cross sections for Xe^+ + Xe at 700 eV

Wavelength (nm)	Upper level	Branching ratio	Cross section ($\times 10^{-18}$cm^2)	Negative Deviation (%)	Positive Deviation (%)	Excitation cross section ($\times 10^{-18}$cm^2)	Notes
788.74	2p1	0.72	1.0918	9.6284	16.4759	1.5164	
823.16	2p6	0.74	58.0919	6.8154	10.8511	78.1856	1
828.01	2p5	1	7.5999	6.8117	17.3969	7.5999	1
834.68	2p3	0.86	5.9345	9.6316	10.4428	6.8766	
840.92	2p7	0.1	3.6569	9.6312	10.6036	36.5686	
881.94	2p8	1	99.0207	9.6306	9.6959	99.0207	
895.23	2p6	0.24	20.3270	9.6300	10.2608	83.6502	
904.54	2p9	0.38	31.9472	6.8400	10.2574	84.2934	2
916.27	2p7	0.9	41.4586	9.6302	9.8055	46.0651	
979.97	2p10	0.98	40.0146	9.6298	9.7184	41.0406	
992.32	2p9	0.62	45.5279	9.6292	9.7685	73.4321	

Table 4.8: Cross sections for Xe^+ + Xe at 800 eV

Wavelength (nm)	Upper level	Branching ratio	Cross section ($\times 10^{-18}$cm^2)	Negative Deviation (%)	Positive Deviation (%)	Excitation cross section ($\times 10^{-18}$cm^2)	Notes
788.74	2p1	0.72	1.0581	9.6285	17.0478	1.4696	
823.16	2p6	0.74	56.4900	6.8219	10.2545	76.0295	1
828.01	2p5	1	7.6070	6.8199	17.6624	7.6070	1
834.68	2p3	0.86	5.5642	9.6313	10.2249	6.4475	
840.92	2p7	0.1	3.4668	9.6310	11.0201	34.6683	
881.94	2p8	1	92.7926	9.6305	9.6897	92.7926	
895.23	2p6	0.24	19.3788	9.6299	10.4098	79.7481	
904.54	2p9	0.38	30.1189	6.8484	10.0355	79.4693	2
916.27	2p7	0.9	38.4576	9.6302	9.8209	42.7307	
979.97	2p10	0.98	33.5009	9.6297	9.7921	34.3599	
992.32	2p9	0.62	42.6799	9.6291	9.7869	68.8385	

Table 4.9: Cross sections for Xe^+ + Xe at 900 eV

Wavelength (nm)	Upper level	Branching ratio	Cross section ($\times 10^{-18}$cm^2)	Negative Deviation (%)	Positive Deviation (%)	Excitation cross section ($\times 10^{-18}$cm^2)	Notes
788.74	2p1	0.72	1.1044	9.6286	16.5659	1.5339	
823.16	2p6	0.74	63.2567	6.8128	9.7541	85.1369	1
828.01	2p5	1	8.4318	6.8115	18.0454	8.4318	1
834.68	2p3	0.86	6.3679	9.6315	10.5049	7.3787	
840.92	2p7	0.1	4.0038	9.6307	11.7728	40.0378	
881.94	2p8	1	104.5640	9.6305	9.6919	104.5640	
895.23	2p6	0.24	22.7820	9.6299	10.4623	93.7531	
904.54	2p9	0.38	33.5798	6.8469	10.0993	88.6009	2
916.27	2p7	0.9	43.5329	9.6302	9.8254	48.3699	
979.97	2p10	0.98	36.6280	9.6297	9.7133	37.5672	
992.32	2p9	0.62	47.5159	9.6291	9.8129	76.6385	

Table 4.10: Cross sections for Xe^+ + Xe at 1000 eV

Number	Note
1	Cross section value is the average of the values from the 735 and 825 micrometer spectra
2	Cross section value is the average of the values from the 825 and 915 micrometer spectra
3	Data unavailable due to insufficient signal-to-noise ratio in the vicinity of this peak

Table 4.11: Cross section table notes

ments is 0.92% in full binning mode. The remainder of the optics contribute negligibly to the error in the intensity measurements. First, the error on the corrected intensity (Equation 3.6) needs to be estimated. The background intensity (B_n) is small compared to the emission intensity (R_n) and so its contribution to the overall error is negligible. The error on the sensitivity function (s_n) results entirely from the CCD measurement error. Other uncertainties in the sensitivity derivation (see Equation 3.4), such as the measurement of the lamp temperature and the uncertainty if the exposure time, are negligible. Therefore, the combined error on I_n is given by:

$$\epsilon(I_n) = \sqrt{\epsilon^2(W_n(x)) + \epsilon^2(R_n(x))} = 0.92\% \cdot \sqrt{2} = 1.3\% \tag{4.2}$$

There are two sources of error on the integrated peak height, P_λ. The first is the measurement error, which is a combination of errors via the addition of $I_\lambda(x)$. The variance is given by:

$$V_{\text{meas}}(P_\lambda) = \sum_x V(I_n(x)) \tag{4.3}$$

The second source of error in P_λ is the extent error which results from the uncertainty in the proper choice of peak extent. It is difficult to quantify this error as the choice of these extents is based on a pragmatic algorithm and does not have a theoretical basis. The true peak—the range in which photons from the transition of interest may fall—is a Voight curve and theoretically extends infinitely in both directions. In an attempt to quantify this error it is assumed that the measureable portion of the true peak does not extend further beyond the detected edge of the peak further than half of the peak width. The total area under the new extent is then taken as the upper bound on the true area of the peak.

$$\epsilon_{\text{ext}}(P_\lambda) = \frac{\sum_{2\times\text{width}} I_\lambda}{\sum_{\text{width}} I_\lambda} - 1 \tag{4.4}$$

These two errors are combined in quadrature to determine the final error on P_λ:

$$V(P_\lambda) = V_{\text{meas}}(P_\lambda) + \left[P_\lambda \epsilon_{\text{ext}}(P_\lambda)\right]^2 \tag{4.5}$$

A result of calculating error in this fashion is that the errors are no longer symmetrical. The contribution to the peak area error resulting from the peak extent determination

is combined into the upper deviation of the error, but not the lower deviation. This asymmetry is propagated to the final cross section error. The results of this algorithm can be viewed in the results. Some peaks show exceptionally large upper deviations, while having modest negative deviations. This suggests that the extent of the peak was not entirely clear due to a large noise floor near the peak edges.

Having calculated an error for the integrated peak intensity, we may now proceed to an estimation of the total cross section error. From Equation 3.16 the fractional error for the cross section is given by:

$$\epsilon(\sigma_\lambda) = \sqrt{\epsilon^2(P_\lambda) + \epsilon^2(G) + \epsilon^2(I_b)} \tag{4.6}$$

The errors in the the peak intensity have already been discussed, and the error in G is listed in Table 3.5. The error in the beam current was determined to be 5%, and is mostly due to current drift over the exposure period. Of these three errors, the error in G usually dominates the others, unless a particular peak is in an unusually noisy region, in which case the extent error may dominate the positive deviation.

For those cross sections where the published result is an average of two micrometer settings, the errors are also combined according to the standard combination of error techniques:

$$\epsilon_{\text{std}}(\sigma_{\text{comb}}) = \sqrt{\frac{1}{4}V(\sigma_1) + \frac{1}{4}V(\sigma_2)}. \tag{4.7}$$

Though it was possible to average two values for every cross section from the 823 nm, 828 nm, and 905 nm lines, This calculation was only performed when the deviations of both lines were comparable. If one of the two values showed a significantly high deviation (typically 50% or greater) it was discarded in favor of the other.

4.3 Xe^{2+} + Xe

It was considerably more difficult to perform the doubly-ionized collision experiment. The main problem is that the ion source is considerably less efficient at producing Xe^{2+} than Xe^{+}. Therefore, the Xe^{2+} beam currents were typically less than ten percent of the Xe^{+} currents for the same beam energy. This implies that the Xe^{2+} emission intensity is also less than ten percent of the corresponding Xe^{+} intensity, assuming comparable cross sections (see Equation 1.29). In fact, the cross sections for Xe^{2+} appear to be much lower than the Xe^{+} cross sections, which further denegrates the situation.

The cross sections determined are plotted in Figure 4.3; however, none of these data are considered reliable. Figure 4.2 shows a portion of the 300 eV Xe^{2+} + Xe collision spectrum. Several of the problems are highlighted. First and greatest, many of the peaks did not exceed the noise floor. This makes it impossible to determine any meaningful results. Secondly, because of the high noise floor in comparison to the total signal height, the true extent of the peak is difficult to determine. Finally, due to the longer exposure times, cosmic rays were much more likely to mar the peaks beyond repair, as may have happened to the 823 nm peak in the figure.

There are a few approaches that could be taken to alleviate the problems in future experiments. The first is immediately obvious from Equation 1.29: increase the

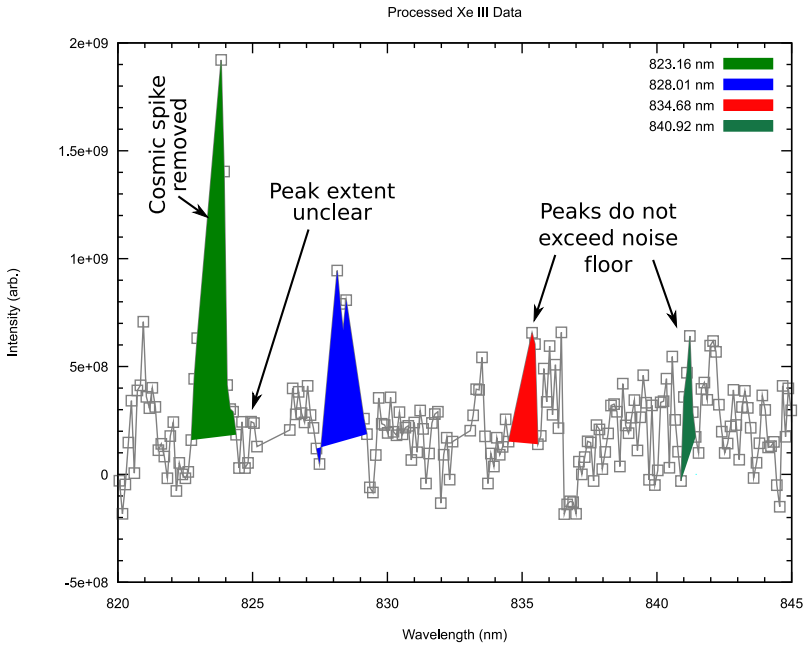

Figure 4.2: Difficulties in processing Xe^{2+} + Xe collision spectra

exposure time. This is not as straightforward as it may sound. Because the detector generates a certain amount of background noise, there is a minimal energy density (time-integrated intensity) that can be detected. To achieve this minimal energy level longer exposures may be taken. However, longer exposures lead to more cosmic spikes which corrupt the signal. One solution to this problem is to take multiple shorter exposures, but this only works if the short exposures are sufficiently long to overcome the noise floor at least a bit. However, through trial-and-error, ideal exposure settings should be achievable using the current equipment.

A second option is to increase the slit width on the spectrograph. Increasing the slit width allows more light into the spectrograph at the expense of spectral resolution. However, so long as one peak is distinguishable from its neighboring peaks, the loss of resolution is not an issue. This solution looks promising given the sparsely populate spectral regime of this study.

Experimentally, the best option is to increase the current level. This may be achievable with the Colutron source through more manipulation of the filament current, anode voltage, and source chamber pressure. However it is more likely that near-optimal beam currents were created in these experiments, and future experiments will not be able to improve the beam current without changing the ion source.

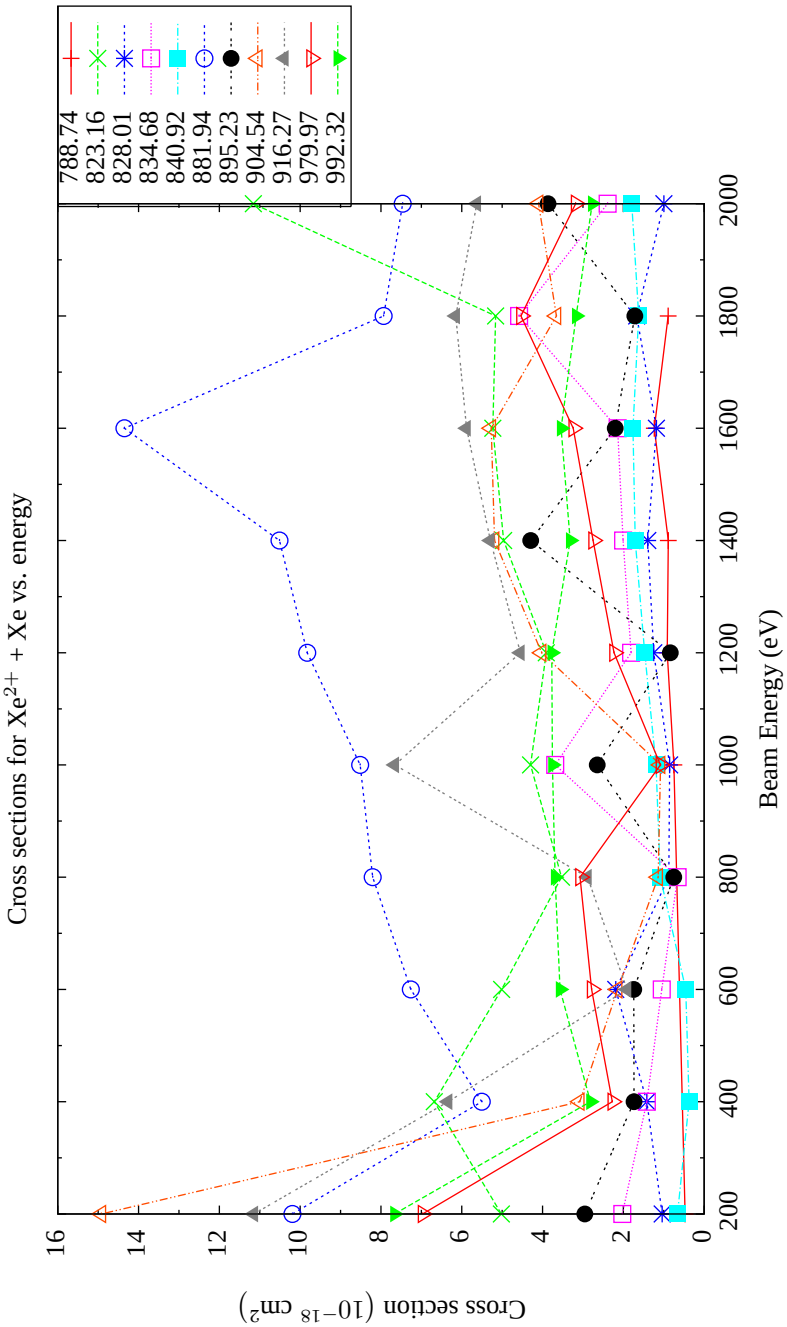

Figure 4.3: Cross sections for Xe^{2+} + Xe versus beam energy. *These data are not reliable.*

Chapter 5

Conclusion

5.1 Review

Ion impact emission cross sections for transitions from the $5p^5 6p$ configuration to the $5p^5 6s$ configuration of neutral xenon occuring in the region from spectral region from 700 nm to 1000 nm have been measured. The data for the singly-ionized impact cross sections show the expected increase in as a function of energy and most values have reasonable errors on the order of 10%. The data for the doubly-ionized impact cross sections are unreliable due to a low signal-to-noise ratio.

5.2 Application example: HET emission simulation

The cross sections from these experiments are of primary use in radiative modeling and the inverse problem of plasma parameter diagnosis via OES. Therefore, it is appropriate to show how these data may be used in such situations, and the effect that they have. In order to do this, I have chosen to further explore the collisional-radiative model put forth by Karabadzhak.[1] As discussed in the introduction (Section 1.2.6) the model is an extension of the coronal equilibrium model. In addition to the processes that the corona model incorporates, Karabadzhak's model also incorporates stepsize excitation of metastables and ion collision excitation.

Dressler has developed a code which implements Karabadzhak's model.[38] This code can be used to simulate the emissions of HET plasma given cross section data for included processes, electron temperature, electron density, neutral density, ion energy, and ion fraction, α_z, for each ionization stage z included in the model. If n_z is the number density of the ionization stage z, the ionization fraction is given by

$$\alpha = \frac{z n_z}{n_e}. \tag{5.1}$$

such that

$$\sum_{z=1}^{Z} \alpha_z = 1 \tag{5.2}$$

Energy (eV)	α
300	0.95
600	0.92
900	0.87

Table 5.1: First ionization fractions for a Hall thruster at various operating voltages

In applying Dressler's simulation, I have neglected the metastable contributions (Equations 1.24 and 1.25) to the the emissions as well as the doubly-charged ion collision excitation (Equations 1.27 and 1.28). This is not to say that these processes are unimportant. The metastable excitation in particular is a very important process in Hall thruster plasma. However, because these simulations are only intended to show the important contribution that ion collisions make in Hall thruster emissions, it is not necessary for all relevant processes to be included.

The rate equation for the model may then be expressed as:

$$I_\lambda = n_0 n_e \left(\langle \sigma_{e_\lambda} v_e \rangle + \alpha \langle \sigma_{i_\lambda} v_i \rangle \right). \tag{5.3}$$

The rate coefficient, $\langle \sigma_{e_\lambda} v_e \rangle$, is defined according to Equation 1.18. The rate coefficient $\langle \sigma_{i_\lambda} v_i \rangle$ is the emission rate resulting from collisions with singly-charged ions. Because the ions in a HET are approximately mono-energetic this may be expressed as

$$\langle \sigma_{i_\lambda} v_i \rangle = \sigma_{i_\lambda}(E) \sqrt{\frac{2E}{m_i}}. \tag{5.4}$$

Because only Xe^+ is considered, only $\alpha = \alpha_1$ is needed. Sample values are given by Hofer[39] and are listed in Table 5.1.

The simulations have been run with sample Hall thruster data from Tables 1.1 and 5.1. The ion impact cross section data used in these simulations are from this thesis (Section 4.1) and electron impact cross sections from Chiu.[24] The model generates line intensities for nine transitions for which complete data were available. Figure 5.1 shows the line intensities at two different conditions for both the corona model and the CR model. These line intensities have been compared over the range of electron temperatures from 0.25 eV to 30 eV by the calculation of the fractional deviation:

$$\text{fractional deviation} = \frac{I_{\text{CR}}}{I_{\text{Coronal}}} - 1. \tag{5.5}$$

Figures 5.2 through 5.4 show the deviation of Karabadzhak's CR model from the traditional coronal equilibrium model at three different ion energies and thus three different thruster operating voltages.

Given the relative magnitudes of the ion and electron cross sections, one would expect that the ions would play a negligible role when electron temperatures, and therefore electron energies, are high. Indeed, these simulations show that the ion contribution is smaller toward the higher temperature regions. However, even at the nominal 30 eV of a Hall thruster chamber, most of the lines still deviate by +10%, suggesting that a model that does not incorporate the ion cross sections will mildly underpredict

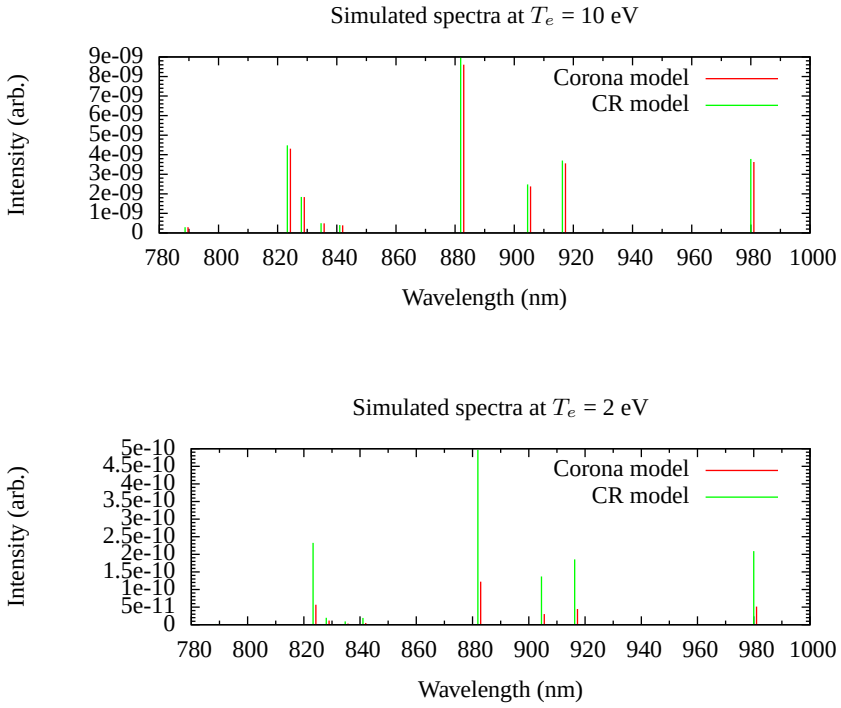

Figure 5.1: Spectra of simulated HET emissions for the corona model and a CR model with 600 eV ions and an electron temperature of $T_e = 10$ eV (top) and $T_e = 2$ eV (bottom)

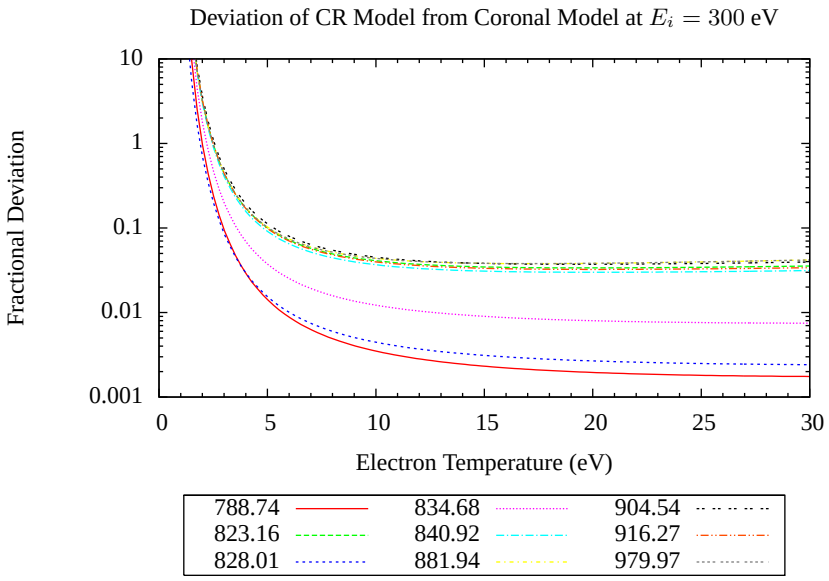

Figure 5.2: Deviation of Karabadzhak's collisional-radiative model including 300 eV ions from the coronal equilibrium model

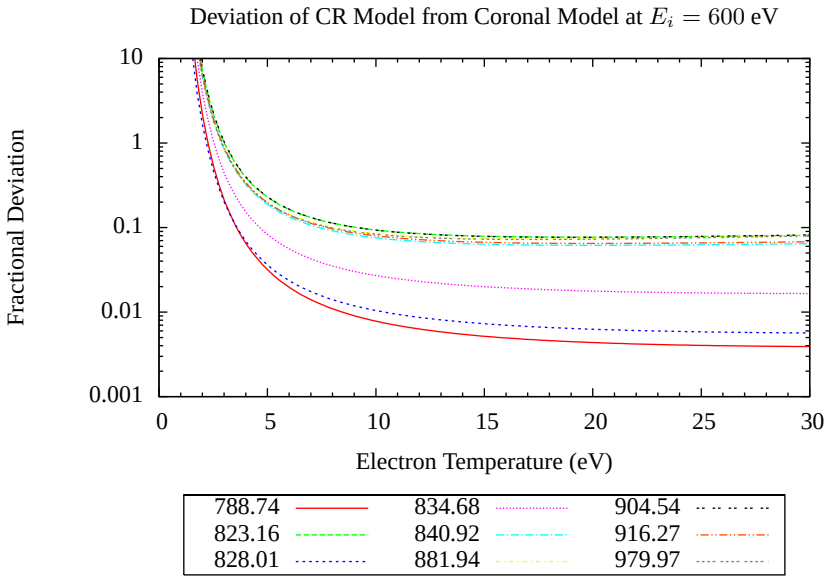

Figure 5.3: Deviation of Karabadzhak's collisional-radiative model with 600 eV ions

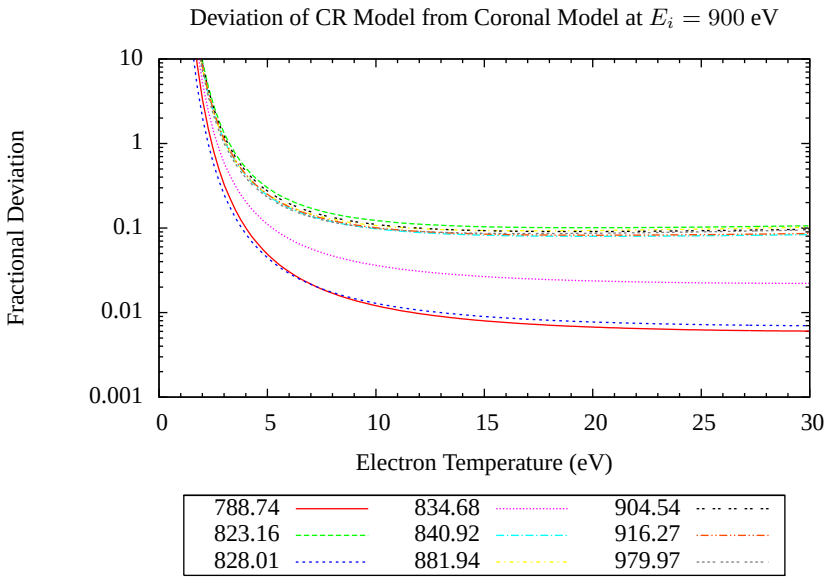

Figure 5.4: Deviation of Karabadzhak's collisional-radiative model with 900 eV ions

emissions, or, conversely, a diagnostic will overpredict the electron temperature and/or electron density.

At the lower temperatures, such as might be expected in the plume, the situation is still worse for the corona model. In this region the cross sections corresponding to the high energy ions begin to vastly outweigh the cross sections corresponding to the low energy electrons. For 300 eV ions, already there is a 20% deviation at $T_e = 5$ eV which rises to a 100% deviation for $T_e = 3$ eV, a typical plume temperature. The situation is worsened for higher ion energies.

The obvious conclusion from these simulations is that the ion collisions play an important role in determining the emissions of HET plasmas, particularly at low electron temperatures. Simple models such as the coronal model that neglect these collisions because "the cross sections are small" are insufficient. Therefore, more complex models are required, and these models may require the cross sections published in this thesis.

Appendix A

Origin of the ten $5p^5 6p$ energy levels

A xenon atom in $5p^5 6p$ excited configuration can be conceived as an ionic core and a single excited electron. Though this is not technically the case, it serves as a sufficient approximation and will suffice for the explanation at hand. Xenon is a large atom, and the outer electrons, particularly the excited electron are better approximated by the j-j coupling scheme, rather than the L-S scheme. That is to say, an individual electron's spin and orbital angular momenta couple more strongly to each other than to the neighboring electrons' momenta.

The momenta of the electrons in the ionic core may give rise to either $^2P_{3/2}$ or $^2P_{1/2}$ configurations.* The unpaired valence electron will have total angular momentum, of either $j_1 = 1/2$ or $j_1 = 3/2$, arising from $j = l + s$ where $l = 1$ and $s = \pm 1/2$. The excited electron's orbital angular momentum, j_2, may take on the same two values. These momenta are added together vectorially according to the rules of quantum mechanics, with the possible values for J being integers between $|j_1 - j_2|$ and $j_1 + j_2$, inclusively. This gives rise to the following combinations:

j_1	j_2	J
1/2	1/2	0, 1
1/2	3/2	1, 2
3/2	1/2	1, 2
3/2	3/2	0, 1, 2, 3

The reader will note that these total ten. Because the $^2P_{1/2}$ ionic core is approximately 1 eV higher in energy than the $^2P_{3/2}$ core, four of these states have a higher energy as compared to the remaining six.

*This is modified spectrographic notation. For the total spin, S, the total orbital angular momentum L, (denoted S=0, P=1, D=2, etc.), and the total angular momentum J, it is given by $^{2S+1}L_J$.[40]

Appendix B

Spectra

This appendix contains charts of the processed spectra for the Xe^{+} + Xe experiments conducted. The data is in photons/s. It should be noted that these units are somewhat arbitrary without considering the volume of the experiment viewed, and the beam current used, as discussed in Section 3.3.

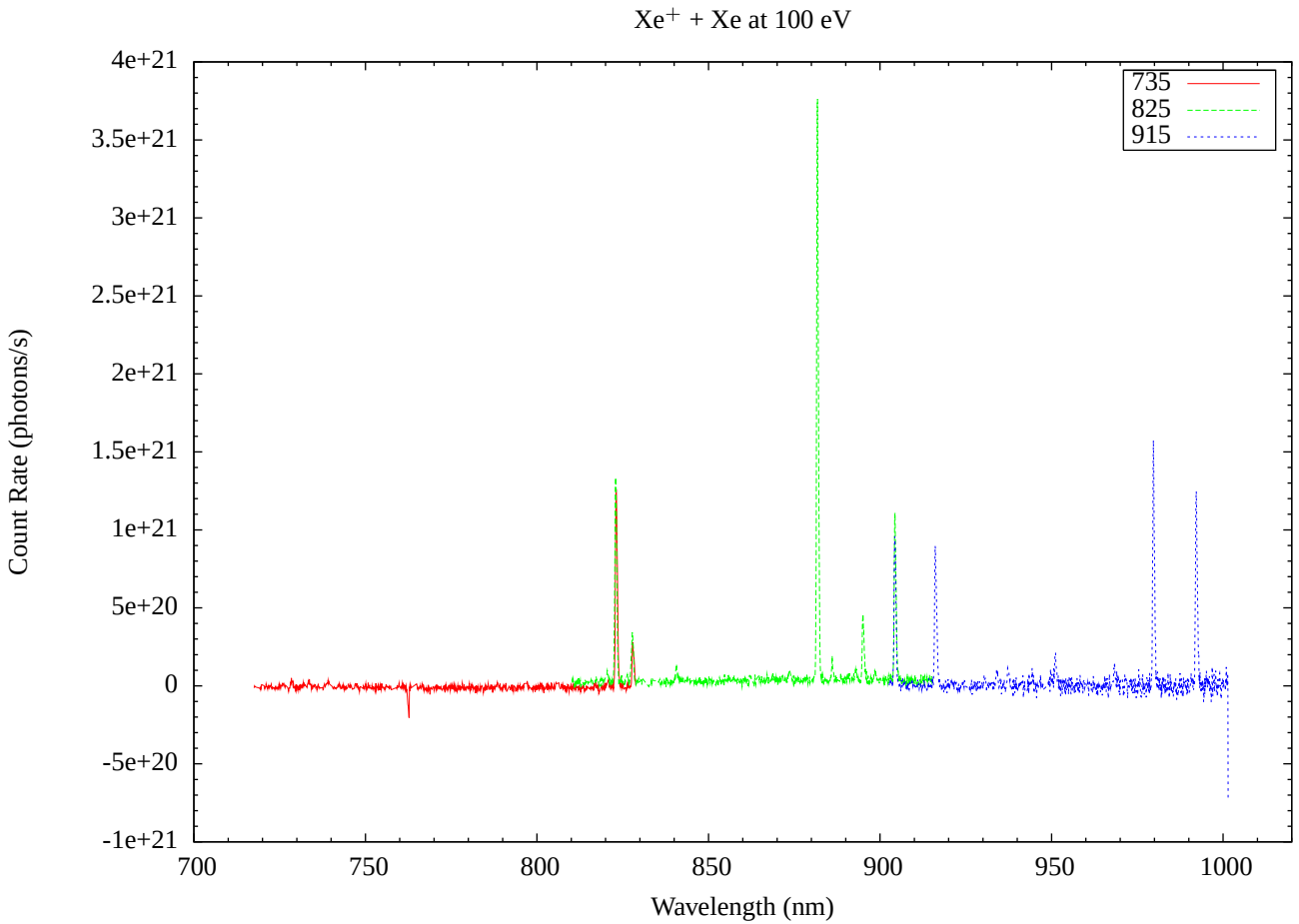
Xe+ + Xe at 100 eV
Count Rate (photons/s)
Wavelength (nm)
735
825
915
4e+21
3.5e+21
3e+21
2.5e+21
2e+21
1.5e+21
1e+21
5e+20
0
-5e+20
-1e+21
700
750
800
850
900
950
1000

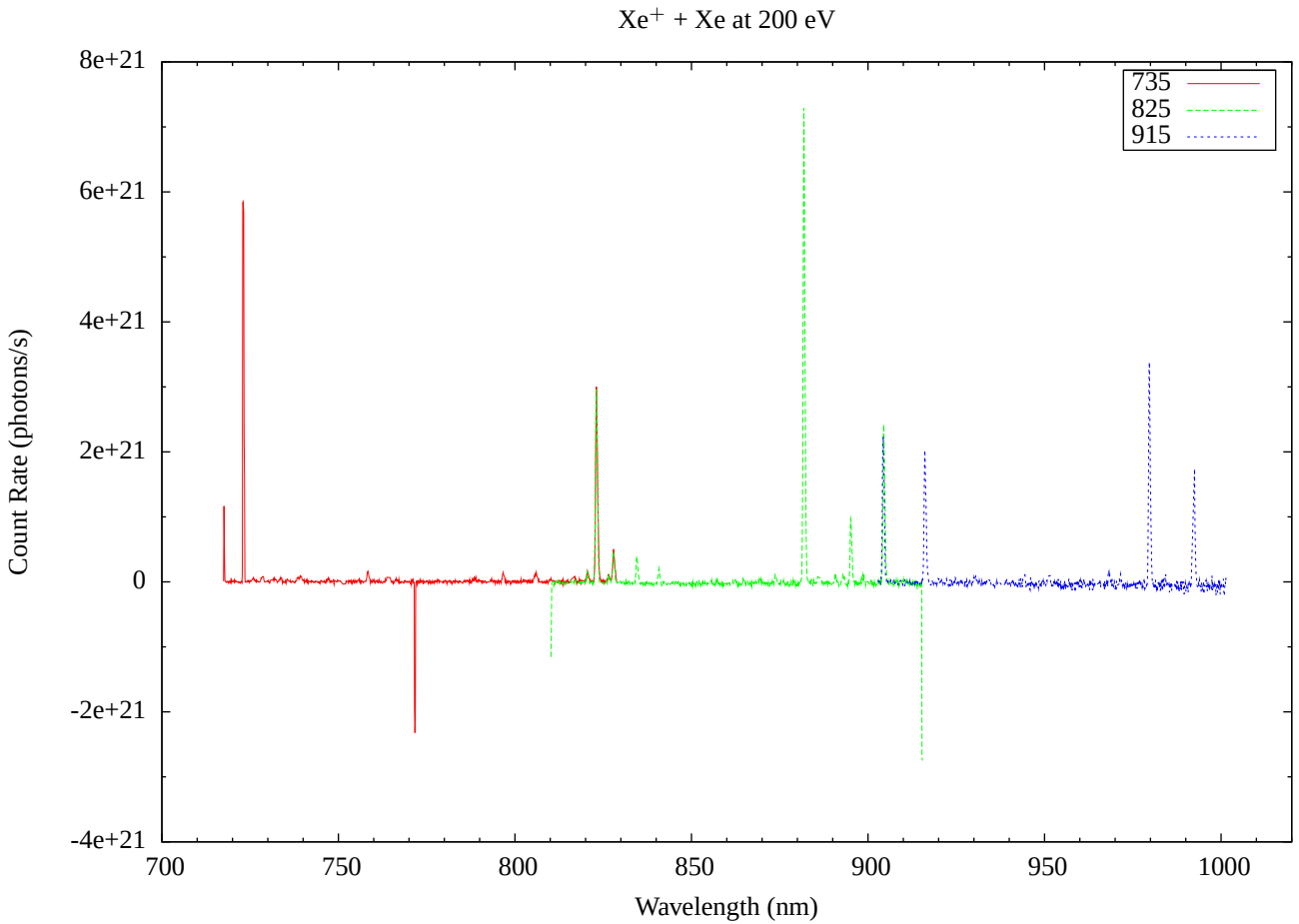
Xe+ + Xe at 200 eV
Count Rate (photons/s)
Wavelength (nm)
735
825
915
8e+21
6e+21
4e+21
2e+21
0
-2e+21
-4e+21
700
750
800
850
900
950
1000

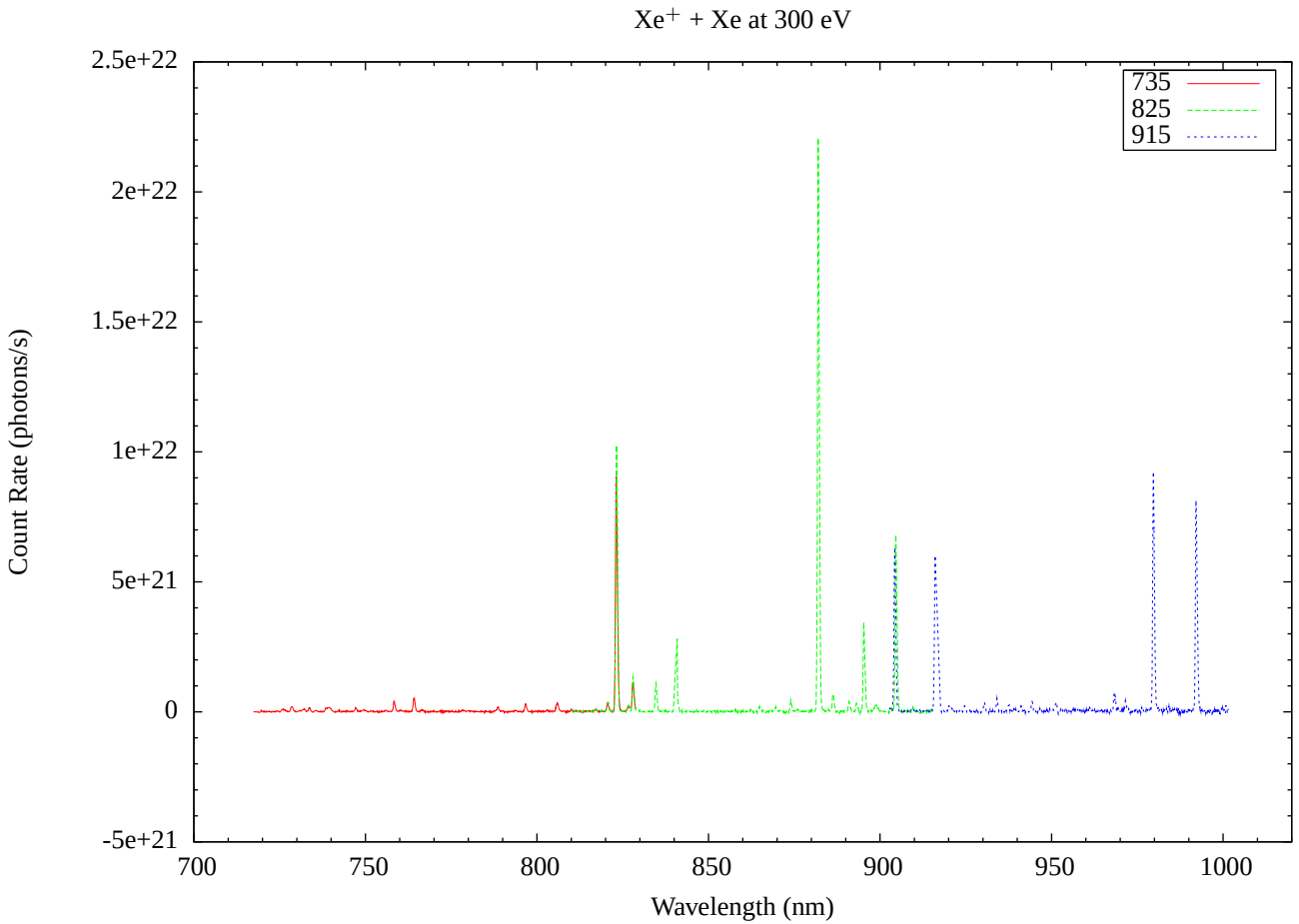
Xe+ + Xe at 300 eV
Count Rate (photons/s)
Wavelength (nm)
735
825
915
2.5e+22
2e+22
1.5e+22
1e+22
5e+21
0
-5e+21
700
750
800
850
900
950
1000

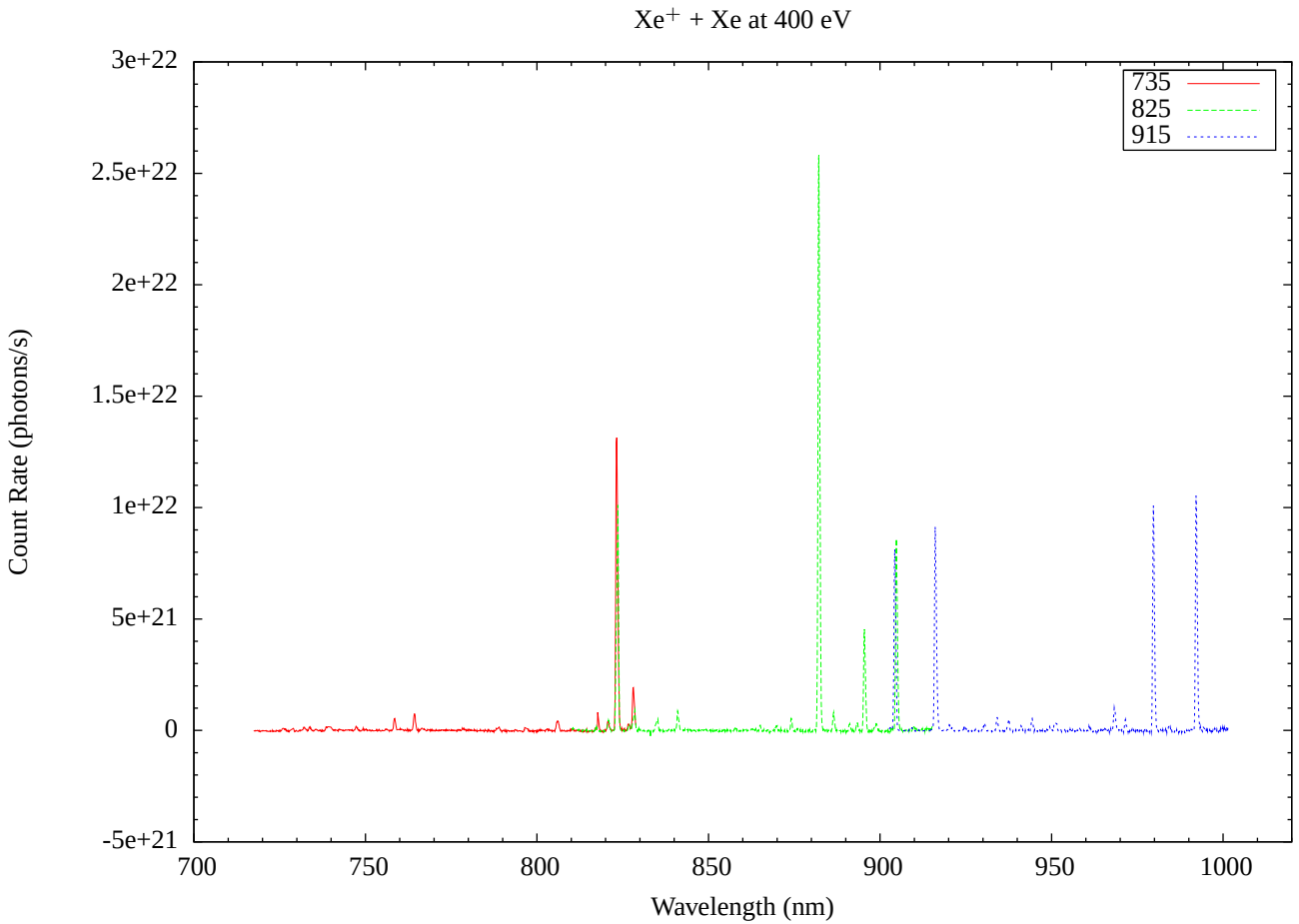
Xe+ + Xe at 400 eV
735
825
915
3e+22
2.5e+22
2e+22
1.5e+22
1e+22
5e+21
0
-5e+21
Count Rate (photons/s)
700
750
800
850
900
950
1000
Wavelength (nm)

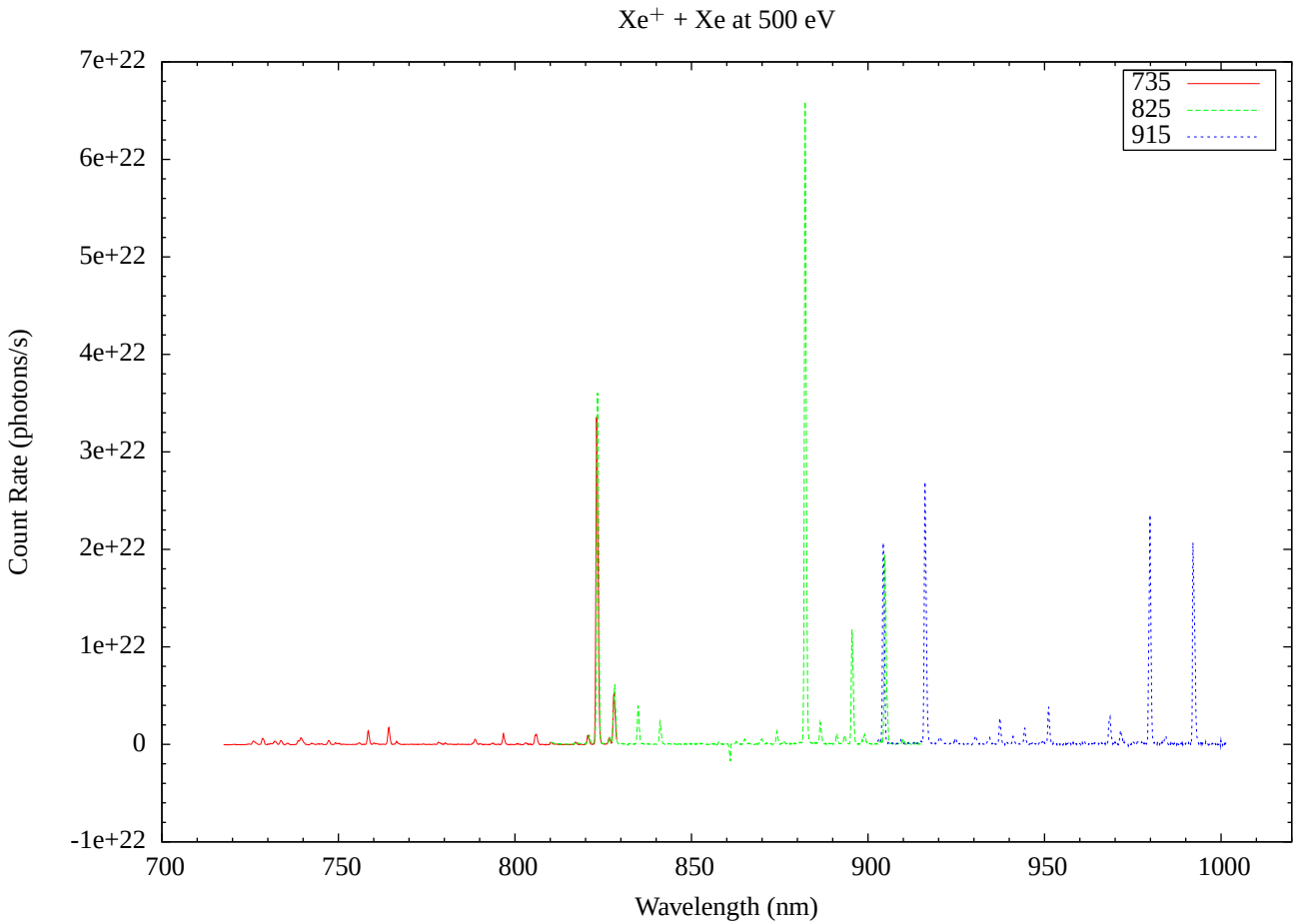
Xe+ + Xe at 500 eV
Count Rate (photons/s)
Wavelength (nm)
7e+22
6e+22
5e+22
4e+22
3e+22
2e+22
1e+22
0
-1e+22
700
750
800
850
900
950
1000
735
825
915

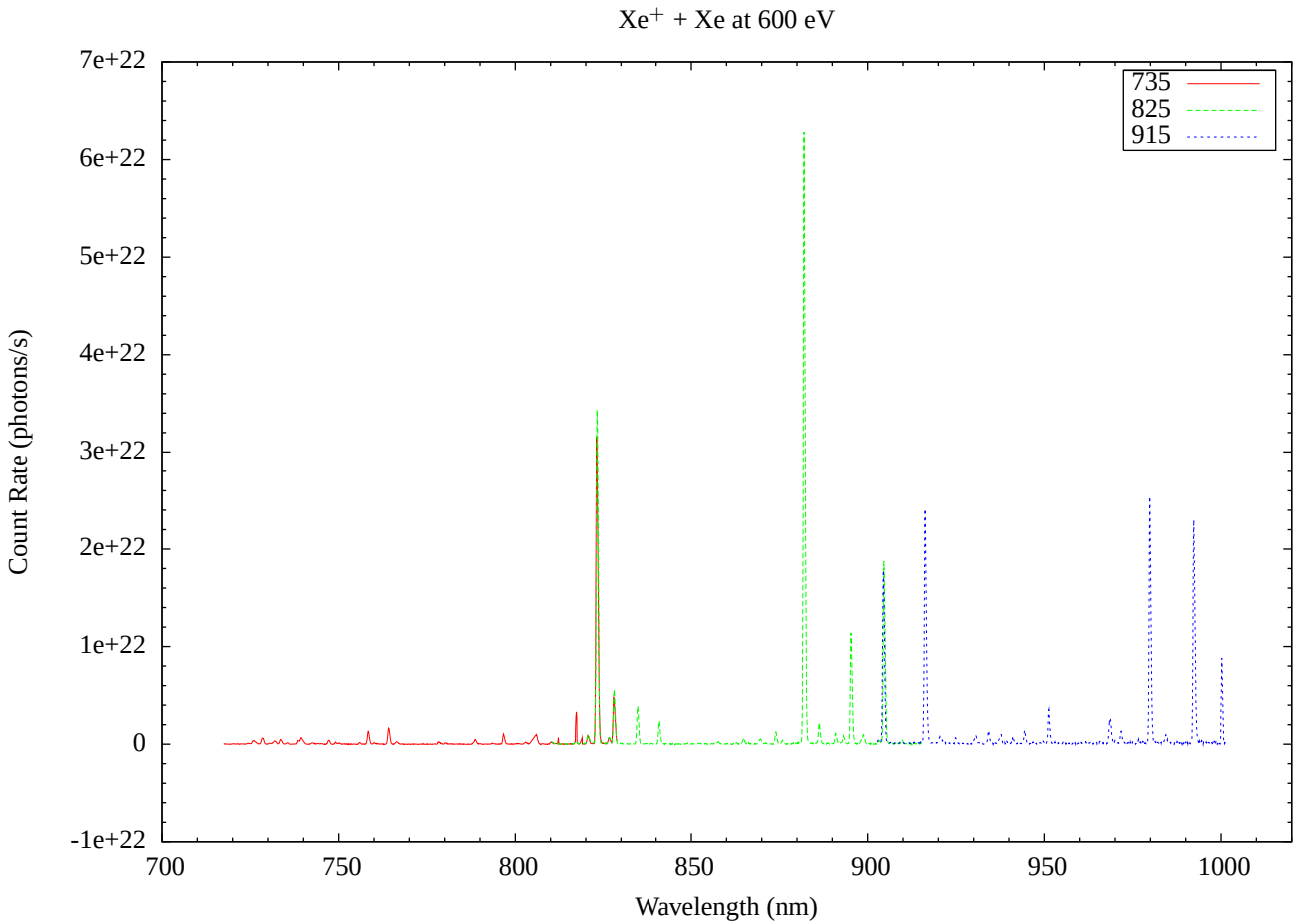
Xe+ + Xe at 600 eV
Count Rate (photons/s)
Wavelength (nm)
735
825
915
7e+22
6e+22
5e+22
4e+22
3e+22
2e+22
1e+22
0
-1e+22
700
750
800
850
900
950
1000

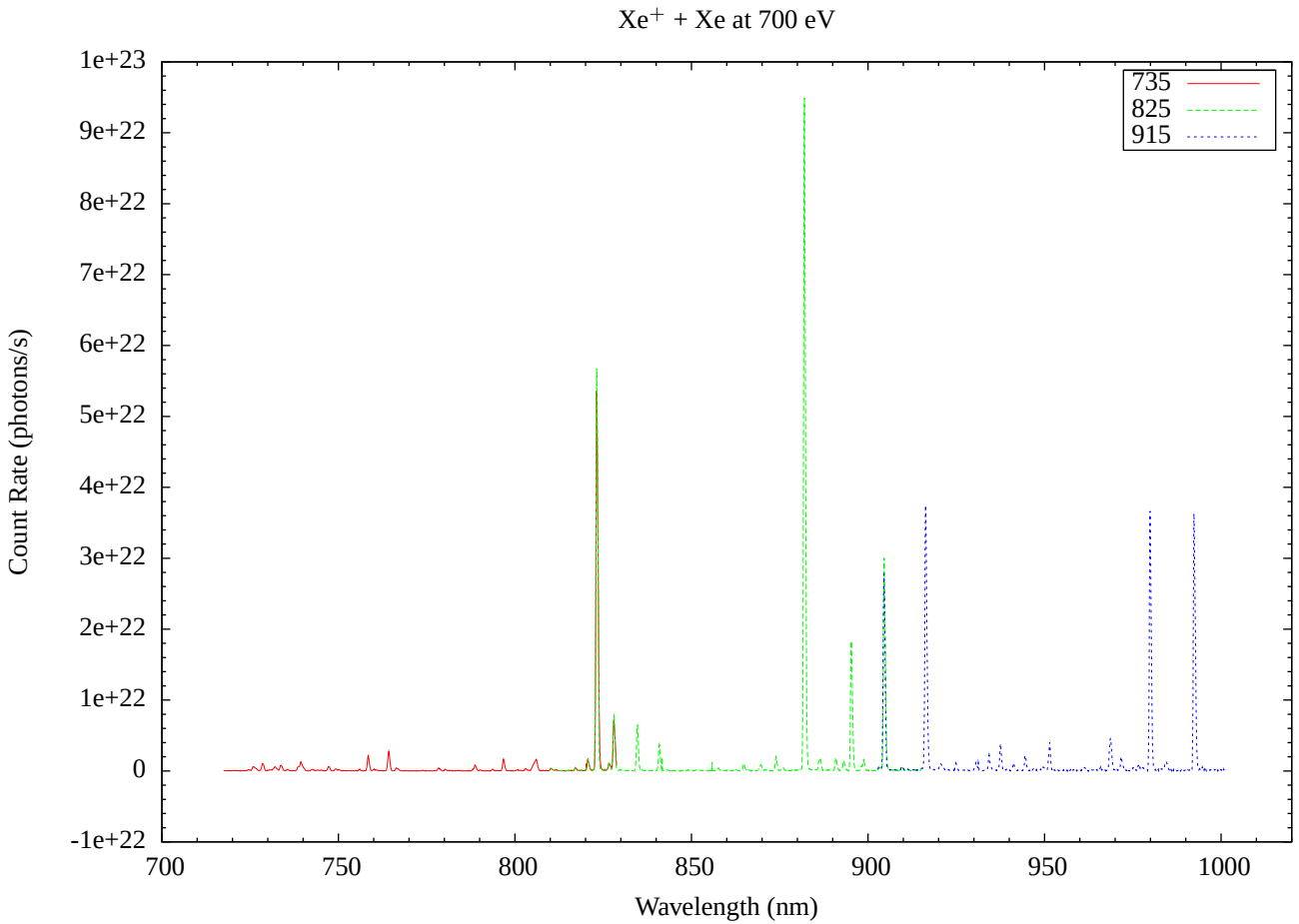
Xe+ + Xe at 700 eV
Count Rate (photons/s)
Wavelength (nm)
735
825
915
1e+23
9e+22
8e+22
7e+22
6e+22
5e+22
4e+22
3e+22
2e+22
1e+22
0
-1e+22
700
750
800
850
900
950
1000

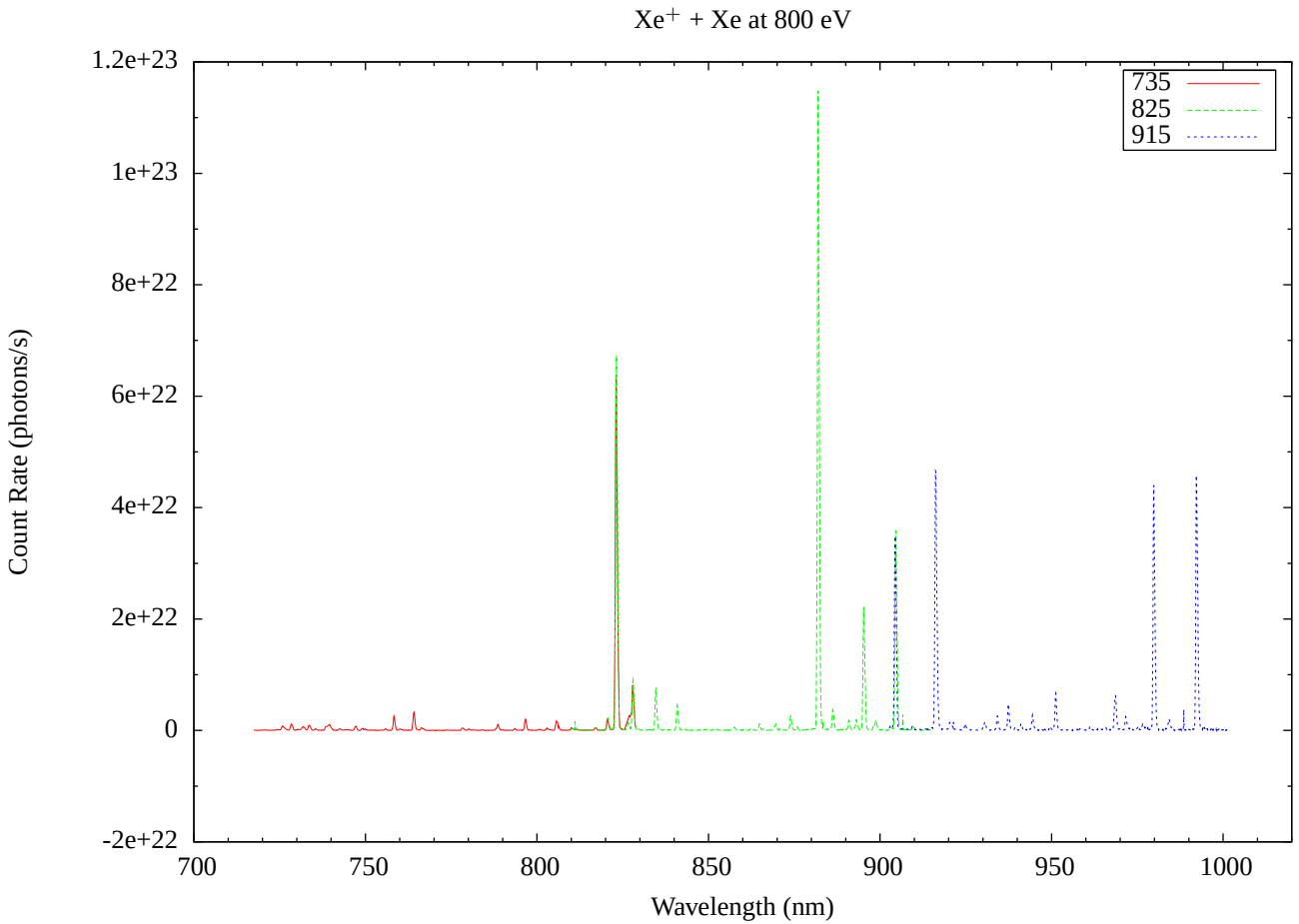
Xe+ + Xe at 800 eV
Count Rate (photons/s)
Wavelength (nm)
735
825
915
1.2e+23
1e+23
8e+22
6e+22
4e+22
2e+22
0
-2e+22
700
750
800
850
900
950
1000

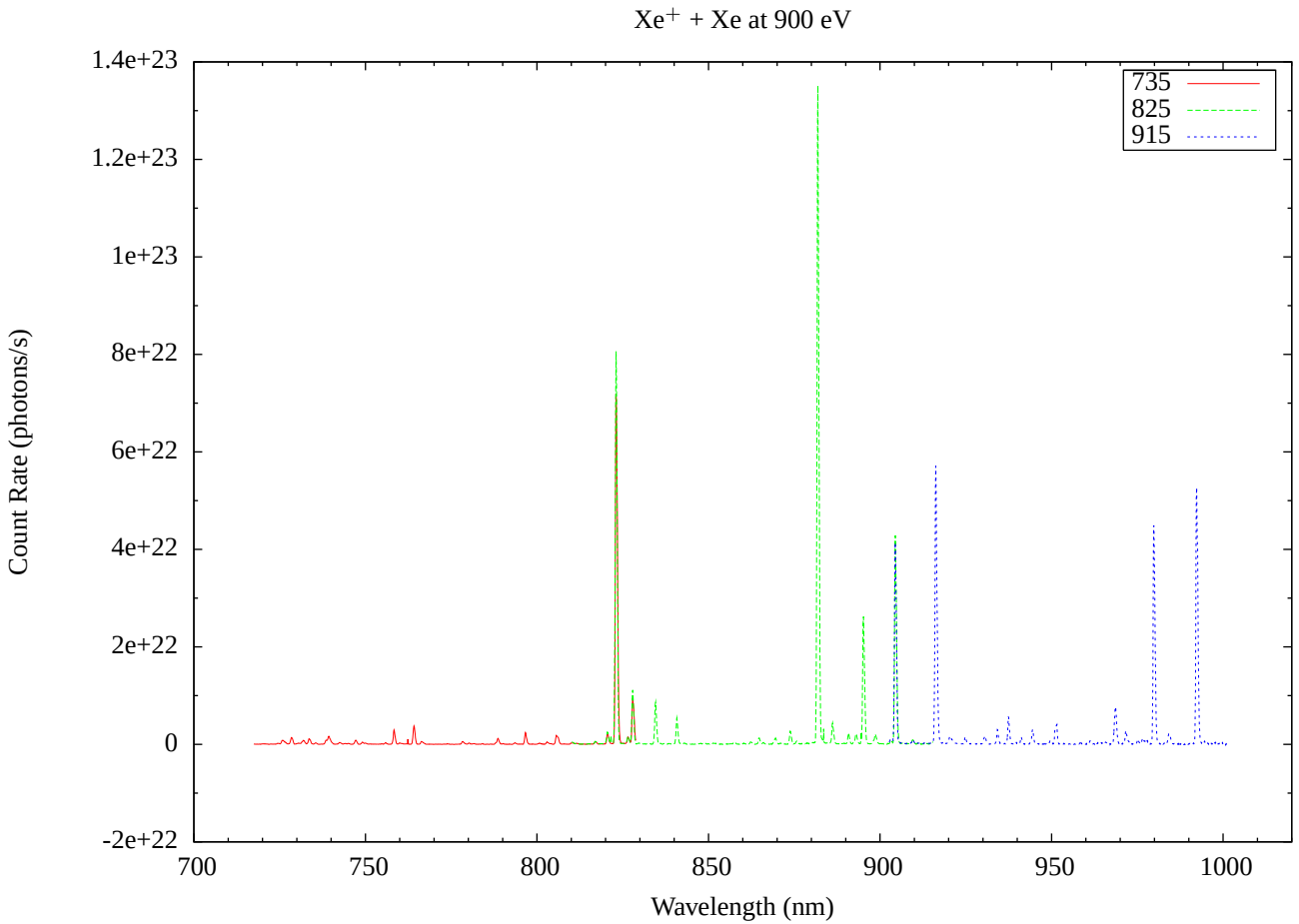
Xe+ + Xe at 900 eV
Count Rate (photons/s)
Wavelength (nm)
735
825
915
1.4e+23
1.2e+23
1e+23
8e+22
6e+22
4e+22
2e+22
0
-2e+22
700
750
800
850
900
950
1000

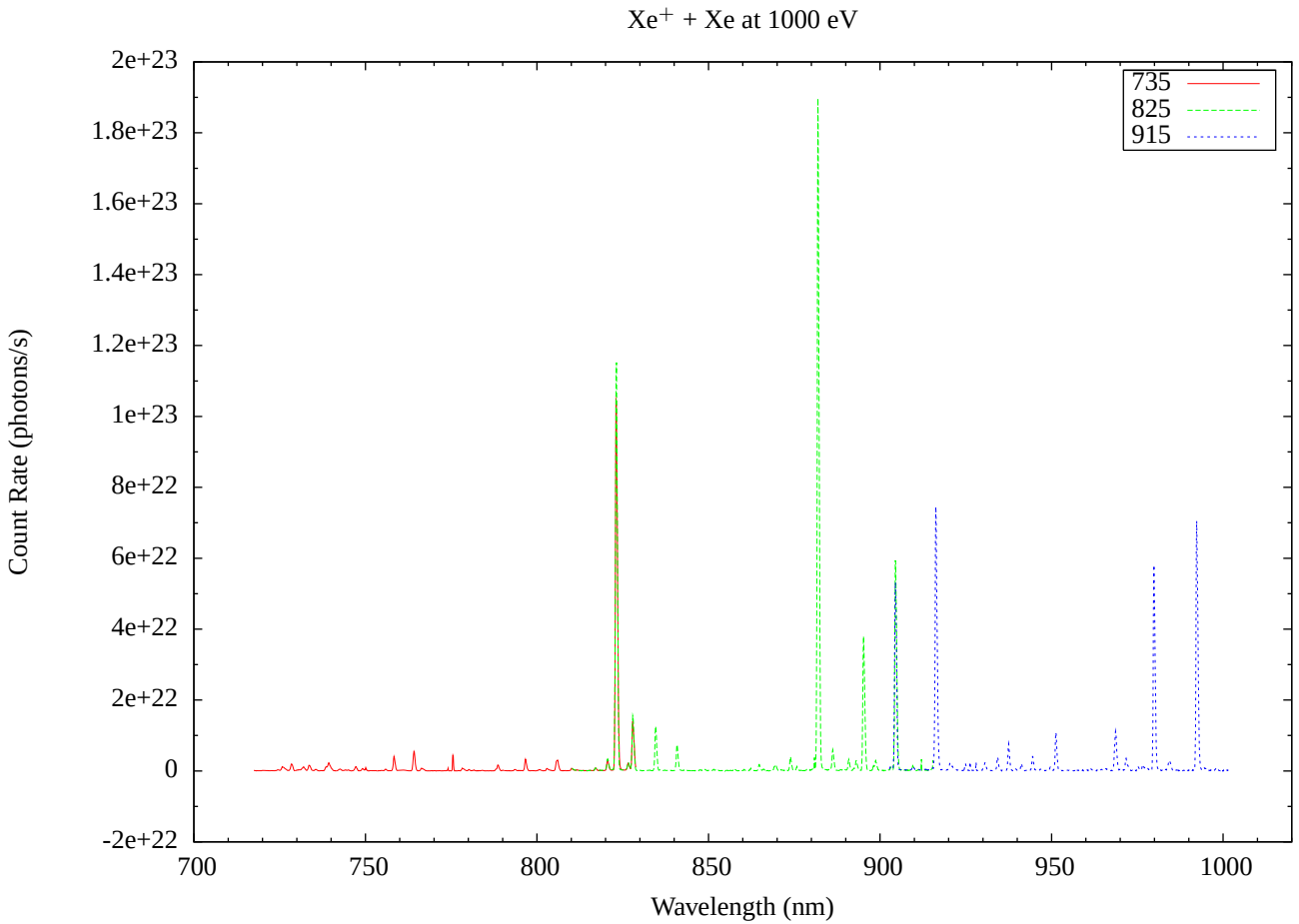
Xe+ + Xe at 1000 eV
Count Rate (photons/s)
Wavelength (nm)
735
825
915
2e+23
1.8e+23
1.6e+23
1.4e+23
1.2e+23
1e+23
8e+22
6e+22
4e+22
2e+22
0
-2e+22
700
750
800
850
900
950
1000

Bibliography

[1] Karabadzhak, G. F., Chiu, Y.-H., and Dressler, R. A., "Passive optical diagnostic of Xe propelled Hall thrusters: Part II: Collisional-radiative model," accepted for publication in the *Journal of Applied Physics*, 2006.

[2] Chen, F. F., *Introduction to Plasma Physics and Controlled Fusion*, Chapter 1: Introduction, Plenum Press, New York, 2nd ed., 1984, pp. 1–18.

[3] Haas, J. M. and Gallimore, A. D., "An Investigation of Internal Ion Number Density and Electron Temperature Profiles in a Laboratory-Model Hall Thruster," Vol. AIAA-00-3422, American Institute of Aeronautics and Astronautics, Huntsville, AL, July 16–19 2000.

[4] Cooper, J., "Plasma spectroscopy," *Rep. Prog. Phys.*, Vol. 29, No. Part I, 1966, pp. 35–130.

[5] Griem, H. R., *Principles of Plasma Spectroscopy*, No. 2 in Cambridge Monographs on Plasma Physics, Cambridge University Press, Cambridge, UK, 1997.

[6] Selwyn, G. S., *Optical Diagnostic Techniques for Plasma Processing*, No. 11 in AVS Monograph Series, The American Vacuum Society Education Committee, New York, 1993.

[7] Fujimoto, T., "A Collisional-radiative model for helium and its application to a discharge plasma," *J. Quant. Spectrosc. Radiat. Trans.*, Vol. 21, No. 5, May 1979, pp. 439–455.

[8] Malyshev, M. V. and Donnelly, V. M., "Trace rare gases optical emission spectroscopy: Nonintrusive method for measuring electron temperatures in low-pressure, low-temperature plasmas," *Phys. Rev. E*, Vol. 60, No. 5, Nov. 1999, pp. 6016–6029.

[9] Sobelman, I. I., *Atomic Spectra and Radiative Transitions*, Chapter 9: Radiative Transitions, No. 12 in Springer Series on Atoms and Plasmas, Springer-Verlag, Berlin, 2nd ed., 1992, pp. 200–302.

[10] Fite, W. L. and Brackmann, R. T., "Collisions of Electrons with Hydrogen Atoms.: II. Excitation of Lyman-Alpha Radiation," *Phys. Rev.*, Vol. 112, No. 4, Nov. 1958, pp. 1151–1158.

[11] Fite, W. L., Stebbings, R. F., and Brackmann, R. T., "Collisions of Electrons with Hydrogen Atoms.: IV. Excitation of Lyman-Alpha Radiation near Threshold," *Phys. Rev.*, Vol. 116, No. 2, Oct. 1959, pp. 356–357.

[12] Stebbings, R. F., Fite, W. L., Hummer, D. G., and Brackmann, R. T., "Collisions of Electrons with Hydrogen Atoms.: V. Excitation of Metastable 2S Hydrogen Atoms," *Phys. Rev.*, Vol. 124, No. 6, Dec. 1961, pp. 2051–2052.

[13] James, G. K., Slevin, J. A., Shemansky, D. E., McConkey, J. W., Bray, I., Dziczek, D., Kanik, I., and Ajello, J. M., "Optical excitation function of H(1s-2p) produced by electron impact from threshold to 1.8 keV," *Phys. Rev. A*, Vol. 55, No. 2, Feb. 1997, pp. 1069–1087.

[14] Hutchinson, I. H., *Principles of Plasma Diagnostics*, Chapter 6: Electromagnetic radiaton from bound electrons, Cambridge University Press, Cambridge, UK, 1987.

[15] McWhirter, R. W. P., *Plasma Diagnostic Techniques*, Vol. 21 of *Pure and Applied Physics*, Spectral Intensities, Academic Press, New York, 1965, pp. 201–264.

[16] Lochte-Holtgreven, W., *Plasma Diagnostics*, Evaluation of Plasma Parameters, North-Holland Publishing Company, Amsterdam, 1968, pp. 135–213.

[17] Chen, F. F., *Introduction to Plasma Physics and Controlled Fusion*, Chapter 7: Kinetic Theory, Plenum Press, New York, 2nd ed., 1984, pp. 225–286.

[18] Bates, D. R., Kingston, A. E., and McWhirter, R. W. P., "Recombination Between Electrons and Atomic Ions. I. Optically Thin Plasmas," *Proc. Roy. Soc. London Ser. A*, Vol. 267, No. 1330, May 1962, pp. 297–312.

[19] Pagnon, D., Touzeau, M., and Lasgorceix, P., "Control of the ceramic erosion by Optical Emission Spectroscopy: parametric studis of SPT100-ML," American Institute of Aeronautics and Astronautics, Fort Lauderdale, CA, July 11–14 2004.

[20] Karabadzhak, G. F., Semenkin, A. V., and Manzella, D. H., "Investigation of TAL optical emissions," *25th IEPC*, Vol. IEPC-97-131, Electric Rocket Propulsion Society, Cleveland, OH, Aug. 24–28 1997.

[21] Guimaraes, F. and Bretagne, J., "Study of an argon magnetron discharge used for molybdenum sputtering. I. Collisional radiative model," *Plasma Sources Sci. Technol.*, Vol. 2, No. 3, Aug. 1993, pp. 127–138.

[22] Guimaraes, F., Almeida, J. B., and Bretagne, J., "Study of an argon magnetron discharge used for molybdenum sputtering. II. Spectroscopic analysis and comparison with the model," *Plasma Sources Sci. Technol.*, Vol. 2, No. 3, Aug. 1993, pp. 138–144.

[23] Leray, P., Bonnet, J., and Pigache, D., "Spacially resolved emission spectroscopy along a SPT channel. Interpretation of data by a collisional-radiative model." *25th IEPC*, Vol. IEPC-97-054, Electric Rocket Propulsion Society, Cleveland, OH, Aug. 24–28 1997.

[24] Chiu, Y.-H., Austin, B. L., Williams, S., and Dressler, R. A., "Passive optical diagnostic of Xe propelled Hall thrusters: Part I: Emission cross sections," accepted for publication in the *Journal of Applied Physics*, 2006.

[25] Hyman, H. A., "Electron-impact?excitation cross sections for the transition $(n-1)p^5ns \rightarrow (n-1)p^5np$ in the rare gases," *Phys. Rev. A*, Vol. 24, No. 2, Aug. 1981, pp. 1094–1095.

[26] Puech, V. and Mizzi, S., "Collision cross sections and transport parameters in neon and xenon," *J. Phys. D: Appl. Phys.*, Vol. 24, No. 11, Nov. 1991, pp. 1974–1985.

[27] Fons, J. T. and Lin, C. C., "Measurement of the cross sections for electron-impact excitation into the $5p^5 6p$ levels of xenon," *Phys. Rev. A*, Vol. 58, No. 6, Dec. 1998, pp. 4603–4615.

[28] Jung, R. O., Boffard, J. B., Anderson, L. W., and Lin, C. C., "Electron-impact excitation cross sections from the xenon J = 2 metastable level," *Phys. Rev. A*, Vol. 72, No. 022723, Aug. 2005.

[29] Filippelli, A. R., Lin, C. C., Anderson, L. W., and McConkey, J. W., *Advances in Atomic, Molecular, and Optical Physics: Cross Section Data*, Vol. 33, Principles and Methods for Measurement of Electron Impact Excitation Cross Sections for Atoms and Molecules by Optical Techniques, Academic Press, San Diego, CA, 1994, pp. 1–62.

[30] Hutchinson, I. H., *Principles of Plasma Diagnostics*, Chapter 3: Plasma particle flux, Cambridge University Press, Cambridge, UK, 1987, pp. 51–86.

[31] Donoso, G. and Martin, P., "Grid effects on velocity analyzers of variable geometry," *Rev. Sci. Inst.*, Vol. 57, No. 8, Aug. 1986, pp. 1501–1506.

[32] Donoso, G., Martin, P., and Puerta, J., "Experimental verification of the grid effects in a velocity analyzer with variable geometry," *Rev. Sci. Inst.*, Vol. 57, No. 8, Aug. 1986, pp. 1507–1511.

[33] Enloe, C. L. and Shell, J. R., "Optimizing the energy resolution of planar retarding potential analyzers," *Rev. Sci. Inst.*, Vol. 63, No. 2, Feb. 1992, pp. 1788–1791.

[34] Enloe, C. L., "High-resolution retarding potential analyzer," *Rev. Sci. Inst.*, Vol. 65, No. 2, Feb. 1994, pp. 507–508.

[35] Sansonetti, J. E. and Martin, W. C., "Atomic Data for Xenon (Xe)," `http://physics.nist.gov/PhysRefData/Handbook/Tables/xenontable1.htm`, March 23 2006.

[36] Incropera, F. P. and DeWitt, D. P., *Fundamentals of Heat and Mass Transfer*, Chapter 12: Radiation: Processes and Properties, John Wiley & Sons, Inc., New York, 2002, pp. 699–788.

[37] Verdeyen, J. T., *Laser Electronics*, Chapter 7, Prentic Hall, Upper Saddle River, NJ.

[38] Dressler, R. A., "HET collisional-radiative model code," April 17 2006, Electronic communication with the author.

[39] Hofer, R. R. and Gallimore, A. D., "Ion Species Fractions in the Far-Field Plume of a High-Specific Impulse Hall Thruster," Vol. AIAA-2003-5001, American Institute of Aeronautics and Astronautics, Huntsville, AL, July 20–23 2003.

[40] Shankar, R., *Principles of Quantum Mechanics*, Chapter 15: Addition of Angular Momenta, Plenum Press, New York, 2nd ed., 1994, pp. 403–429.